

Synthesis and Dual Excitonic Emission of Sn-Iodide Layered Hybrid Perovskites

A Thesis

submitted to

Indian Institute of Science Education and Research (IISER), Pune

In partial fulfilment of the requirements for the

BS-MS Dual Degree Programme

by

Nawale Vaibhav Vilas



Indian Institute of Science Education and Research (IISER), Pune

Dr. Homi Bhabha Road,

Pashan, Pune 411008, INDIA.

April 2020

Supervisor: Dr. Angshuman Nag

Associate Professor, Department of Chemistry

IISER Pune

All rights reserved

Certificate

This is to certify that this dissertation entitled "**Synthesis and Dual Excitonic Emission of Sn-Iodide Layered Hybrid Perovskites**" towards the partial fulfilment of the BS-MS dual degree programme at the Indian Institute of Science Education and Research, Pune represents study/work carried out by **Nawale Vaibhav Vilas** at Indian Institute of Science Education and Research under the supervision of **Dr. Angshuman Nag**, Associate Professor, Department of Chemistry, during the academic year 2019-2020.



Student

Nawale Vaibhav Vilas



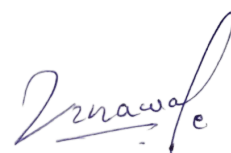
Supervisor

Dr. Angshuman Nag

29/03/2020

Declaration

I hereby declare that the matter embodied in the report entitled “**Synthesis and Dual Excitonic Emission of Sn-Iodide Layered Hybrid Perovskites**” are the results of the work carried out by me at the Department of Chemistry, Indian Institute of Science Education and Research, Pune, under the supervision of **Dr. Angshuman Nag** and the same has not been submitted elsewhere for any other degree.



Nawale Vaibhav Vilas

Date: 29/03/2020

This thesis is dedicated to my friends.

Acknowledgements

I am personally thankful to IISER Pune for providing a wonderful learning experience during my undergraduate studies. I learned and enjoyed a lot during my 5-year journey here. I would cherish each and every moment of my stay here at IISER Pune.

First and foremost, I would like to express my sincere gratitude to Dr. Angshuman Nag for providing me a wonderful opportunity to carry out my final year thesis project under his supervision. His patience, enthusiasm and extensive knowledge have helped me a lot to tackle various scientific problems and also stimulated my interest in the field of research. His guidance has not only helped me to carry out a thesis project successfully but also promote my professional growth.

I would also like to thank my thesis advisory committee member Dr. Nirmalya Ballav for his insightful comments and critical questions during the assessment of my project and that really helped me to improve my quality of work and thus overall quality of the thesis.

I am also very thankful to Mr. Ravinder Malothu (single crystal XRD operator, IISER Pune) for providing me timely slots and helping out in a collection of the data.

I am also grateful to Dr. Arnab Mukherjee and Dr. Nirmalya Ballav for offering me a summer internship in their groups during my undergraduate year. It exposed me to a wide area of research and really sparked my love for science. I am thankful to Atul Thakur from Dr. Mukherjee's group and Debashree Roy from Dr. Ballav's with whom I have worked and learned many things.

Also, I would like to thank my labmates at the Dr. Angshuman Nag Lab without whom research would have been tedious. I am fortunate to have such helpful fellow labmates who helped and guided me along my research journey at Dr. Nag's lab. We worked together at nights and had enjoyable tea sessions and brainstorming group discussions which were really fun and kept me motivated. I would like to especially mention Mr. Tariq and Mr. Rayan, who taught me perovskite synthesis, handling of instruments at the beginning of my project. We had very fruitful discussions that helped me establishing the basics and getting the concepts cleared.

I would also like to thank Mr. Vikash Kumar Ravi, who was always present to help me regarding various things apart from the research. He enlightened me with the virtue of his work that helped me to possess the right mindset for research and develop scientific temperament.

I would also like to thank my family, especially my sister, she has always been very supportive. Last but not least, I am very thankful to my amazing friends as because of them life is exciting. Even in harder times, they were with me and encouraged me to improve myself.

Table of Contents

Abstract	1
1. Introduction	2
2. Experimental Section	7
2.1 Chemicals.....	7
2.2 Synthesis Methods	7
2.2.1 Synthesis of $((\text{C}_6\text{H}_5)_2\text{C}_2\text{H}_4\text{NH}_3)_2\text{SnI}_4$, i.e. $(\text{PEA})_2\text{SnI}_4$ single crystal	7
2.2.2 Synthesis of $(\text{C}_4\text{H}_9\text{NH}_3)_2\text{SnI}_4$, i.e. $(\text{BA})_2\text{SnI}_4$ single crystal	7
2.2.3 Synthesis of $(\text{C}_6\text{H}_{13}\text{NH}_3)_2\text{SnI}_4$, i.e. $(\text{HA})_2\text{SnI}_4$ single crystal	8
2.2.4 Synthesis of $(\text{C}_8\text{H}_{17}\text{NH}_3)_2\text{SnI}_4$, i.e. $(\text{OA})_2\text{SnI}_4$ single crystal	8
2.2.5 Synthesis of $(\text{C}_6\text{H}_{16}\text{N}_2)\text{SnI}_4$, i.e. 4-AMPSnI ₄ single crystal	8
2.2.6 Synthesis of $(\text{C}_6\text{H}_{16}\text{N}_2)\text{PbI}_4$, i.e. 4-AMPPbI ₄ single crystal	9
2.2.7 Exfoliated $(\text{PEA})_2\text{SnI}_4$, $(\text{BA})_2\text{SnI}_4$, $(\text{HA})_2\text{SnI}_4$ and $(\text{OA})_2\text{SnI}_4$	9
2.3 Characterization Techniques	9
2.3.1 Single crystal X-ray diffraction	9
2.3.2 Powder X-ray diffraction	9
2.3.3 UV-vis absorption spectroscopy	10
2.3.4 UV-vis-NIR diffused reflectance spectroscopy	10
2.3.5 Steady-state photoluminescence (PL) spectroscopy and PL decay dynamics	10
2.3.6 Scanning electron microscopy	10
2.3.7 Atomic force microscopy	10
3. Results and Discussion	10
3.1 Characterisation of $(\text{PEA})_2\text{SnI}_4$ single crystal	10
3.2 Photophysical study of $(\text{PEA})_2\text{SnI}_4$ single crystal	12
3.3 Exfoliated $(\text{PEA})_2\text{SnI}_4$	13

3.4 Characterisation of the (BA) ₂ SnI ₄ , (HA) ₂ SnI ₄ and (OA) ₂ SnI ₄ single crystals.....	14
3.5 Photophysical study of (BA) ₂ SnI ₄ , (HA) ₂ SnI ₄ and (OA) ₂ SnI ₄ single crystals	17
3.6 Characterization of 4-AMPPbI ₄ single crystals	21
3.7 Photophysical study of 4-AMPPbI ₄	23
3.8 Characterization of 4-AMPSnI ₄ single crystals	25
3.9 Photophysical study of 4-AMPSnI ₄	25
4. Conclusions.....	27
References	27

List of Figures

1. The schematic shows the derivation of the crystal structure of hybrid organic inorganic perovskites (HOIP) from oxide perovskites	2
2. Representation of single layer of <100> orientated HOIP	4
3. Structure of ((C ₆ H ₅)C ₂ H ₄ NH ₃) ₂ PbI ₄ with alternating organic and inorganic layers forming the multiple quantum well (MQW) structures	5
4. Morphology and structural characterisation of (PEA) ₂ SnI ₄	11
5. Photophysical study of (PEA) ₂ SnI ₄ single crystal.....	12
6. PL decay dynamics recorded on (PEA) ₂ SnI ₄ single crystal.....	13
7. Exfoliated (PEA) ₂ SnI ₄	14
8. Structural characterization of (BA) ₂ SnI ₄ , (HA) ₂ SnI ₄ and (OA) ₂ SnI ₄	15
9. Ball and stick representation of (BA) ₂ SnI ₄ , (HA) ₂ SnI ₄ and (OA) ₂ SnI ₄	15
10. Photophysical study of (BA) ₂ SnI ₄ , (HA) ₂ SnI ₄ and (OA) ₂ SnI ₄	18

11. PL decay dynamics measured at both emission peaks of (BA) ₂ SnI ₄ , (HA) ₂ SnI ₄ and (OA) ₂ SnI ₄	20
12. Morphology and structural characterisation of 4-AMPPbI ₄	22
13. Photophysical study of 4-AMPPbI ₄	24
14. PL decay dynamics recorded for 4-AMPPbI ₄ microcrystals.....	24
15. PXRD pattern of 4-AMPSnI ₄ single crystal.....	25
16. Photophysical study of 4-AMPSnI ₄	26

List of Tables

1. Crystal data and structure refinement for (PEA) ₂ SnI ₄	11
2. Crystal data and structure refinement for (BA) ₂ SnI ₄ , (HA) ₂ SnI ₄ and (OA) ₂ SnI ₄	16
3. Comparison of dual excitonic emissions for Sn and Pb RP perovskite systems	21
4. Crystal data and structure refinement for 4-AMPPbI ₄	23
5. Comparison of dual excitonic emissions for RP and DJ perovskite systems	26

Abstract:

In recent years both three-dimensional (3D) and two-dimensional (2D) hybrid perovskites drew significant attention for their excellent optoelectronic properties and solution processibility. In difference to 3D perovskites like $\text{CH}_3\text{NH}_3\text{PbI}_3$, 2D perovskites like $((\text{C}_6\text{H}_5)\text{C}_2\text{H}_4\text{NH}_3)_2\text{PbI}_4$ have less stringent structural requirements, which allows more flexibility in organic and inorganic compositions of 2D perovskites. Subsequently, longer hydrophobic organic molecules can be used in 2D perovskites providing better moisture stability. In this thesis, we prepared different Sn-I based 2D hybrid perovskites, which remain significantly stable. Note that in 3D Sn-I perovskites, Sn (II) rapidly oxidizes to Sn (IV) destroying the 3D perovskite structure. Two different varieties, namely Ruddlesden-Popper phase with the generic formula $(\text{R-NH}_3)_2\text{SnI}_4$ and Dion-Jacobson phase with generic formula $(\text{NH}_3\text{-R-NH}_3)\text{SnI}_4$ with varying hydrocarbon groups R (both alkyl and aryl) are prepared. Samples are mainly in the form of centimetre sized single crystalline flakes, along with microcrystals and some physically exfoliated samples.

After the synthesis and structural characterization, the major emphasis of the thesis is in understanding their excitonic absorption and emission. The hybrid Sn-I layered perovskites show repeating quantum well structure. The charge carriers are confined in the semiconducting inorganic Sn-I layers, which are separated from each other by insulating organic layers. This quantum well structure leads to high excitonic binding energies manifesting sharp and intense excitonic absorption and emission. We find a very unusual observation where the single crystals of Sn-I layered perovskites exhibit two excitonic emissions. Comparison of these Sn-I samples with layered Pb-I perovskites shows all the samples exhibit such dual excitonic emission. These results suggest the possibility of interactions between Sn-I layers at some parts of the crystals. Understanding of this unusual property is required to optimize the optoelectronic applications of hybrid layered perovskites.

1. Introduction:

Perovskite is the crystal structure of calcium titanium oxide mineral, with the chemical formula of CaTiO_3 . This mineral was first discovered in the Russian Ural Mountains by German Mineralogist Gustave Rose and named in honour of the Russian mineralogist Count L.A. Perovski.¹ Now many other known compounds show perovskite structure similar to CaTiO_3 . The general formula of perovskite is ABX_3 , where A and B are two different sizes of cations and X is anion coordinated to cation B. The cation B is coordinated to six other X anion which forms BX_6 octahedra. Such octahedra connected with each other in the corner sharing fashion and build the 3D framework. The A-site cations are generally larger in size compare to B, and occupy the space in between the cavities formed by eight corner sharing octahedra (Figure 1(a)).²

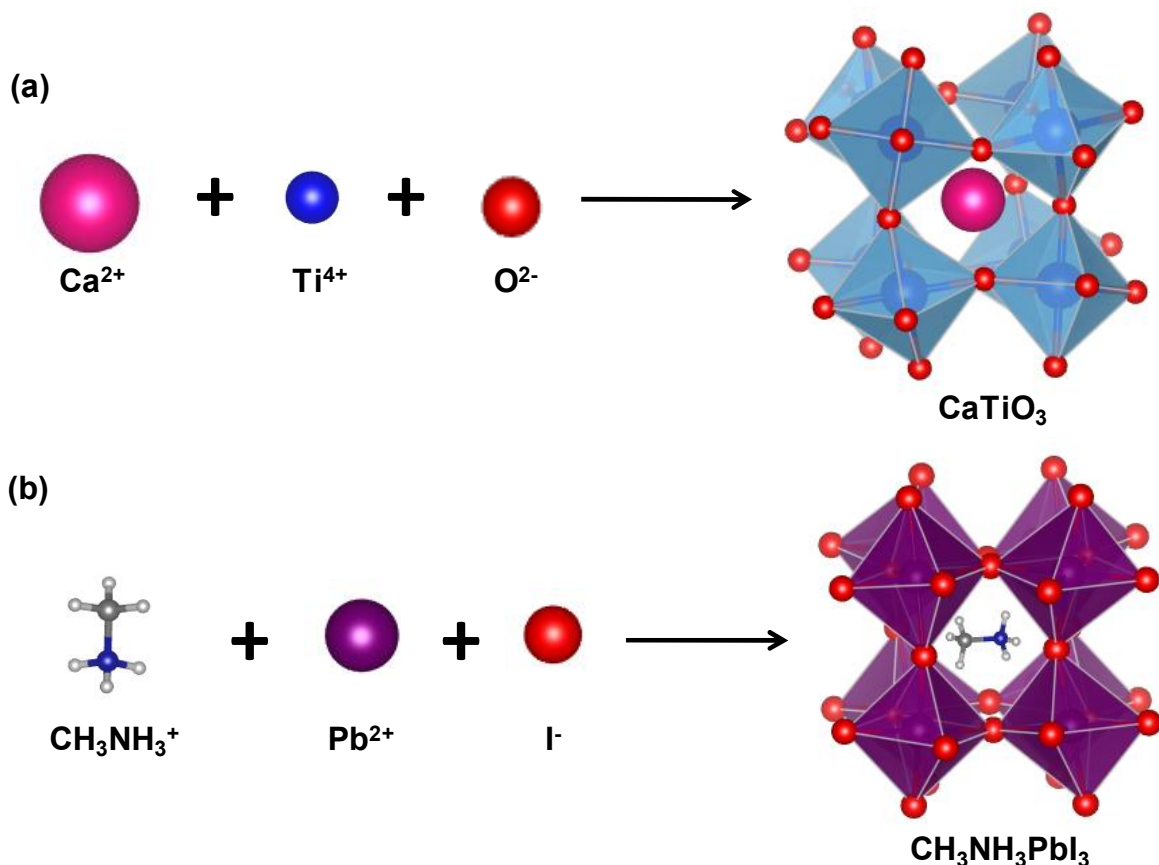


Figure 1. The schematic shows the derivation of the crystal structure of Hybrid organic inorganic perovskites (HOIP) from oxide perovskites. (a) Example of oxide perovskite, CaTiO_3 and (b) example of HOIP, $\text{CH}_3\text{NH}_3\text{PbI}_3$.

An organic compound possesses several useful properties, including structural diversity, plasticity, efficient luminescence, and ease of processing. On the other hand, inorganic material like oxide perovskites has its own set of advantages such as good electrical mobility, mechanical hardness and heat resistance, bandgap tunability and magnetic or dielectric transitions. Hybrid organic inorganic perovskites (HOIP) provide the platform to combine the properties of these two chemical realms within the same entity.³ These hybrid organic inorganic perovskites are the subclass of ABX_3 materials consist of the organic cation (e.g. $CH_3NH_3^+$) occupying the A site position in the crystal structure (Figure 1(b)). In HOIP, B is divalent cation like Pb^{2+} , Sn^{2+} , Ge^{2+} whereas X is monovalent anion including the Cl^- , Br^- , I^- . The A-site can be occupied by molecular blocks like $CH_3NH_3^+$ and $NH_2CH=NH_2^+$. This modification provides not only structural flexibility but also introduces new functionalities over the conventional inorganic perovskites. An existing vast variety of organic cations and metal salts offers enormous possibilities of HOIP. Due to this, most of the elements from the periodic table are part of perovskite systems. The ratio of ionic sizes that can tolerate closed packed perovskite structure is denoted by Goldschmidt Tolerance Factor (t). The tolerance factor for the system in which A, B, and X ions are in close contact is given by the equation, $t = (R_A + R_X) / \sqrt{2}(R_B + R_X)$, where R_B denotes Shannon radius of B-site metal ion, R_A , R_X is the effective radius of A-site cation and X-site anion respectively. Typically for most of the cubic perovskite systems, the tolerance factor is $0.8 \leq t \leq 0.9$.⁴ For $t=1$, maximum R_A value for organic cation is approximately 2.6 Å (i.e. distance equivalent to less than three C-C bond distances) expected to fit into the 3D structure (Figure 1(b)).⁵

Conceptually specific cuts of 3D perovskites give rise to lower dimensional perovskite structures. We can imagine 3D perovskite is cut into one layer thick slices along $\langle 100 \rangle$ direction and separated them apart.⁶ The general formula of $\langle 100 \rangle$ oriented perovskite is $(A_2'A_{n-1}B_nX_{3n+1})$, where A' is longer chain organic cation and n is a number of inorganic layers. Such layered perovskites consist of an alternative arrangement of organic (insulating) and inorganic semiconducting layers. The inorganic layers consist of the BX_4^{2-} layers of corner sharing metal halide octahedra which are separated by organic cation bilayers (for monovalent cation) or monolayers (for divalent cation) (Figure 2).⁷ These two layers are held together by the Coulombic and hydrophobic forces which maintain the structure. In layered

perovskite, there is no size restriction on organic cation, since the cage into which organic cation must fit is not confined in three dimensions. Hence, 2D layered perovskites can accommodate much larger and complex organic cations.⁸

For successful incorporation of organic cation within layered perovskite, several guidelines need to follow. First, the organic molecule must contain one or more cationic groups that can ionically interact with the inorganic framework without sterically interfering with halide ions. Second, there should be effective hydrogen bonding of the terminal amine group with an extended inorganic framework.³

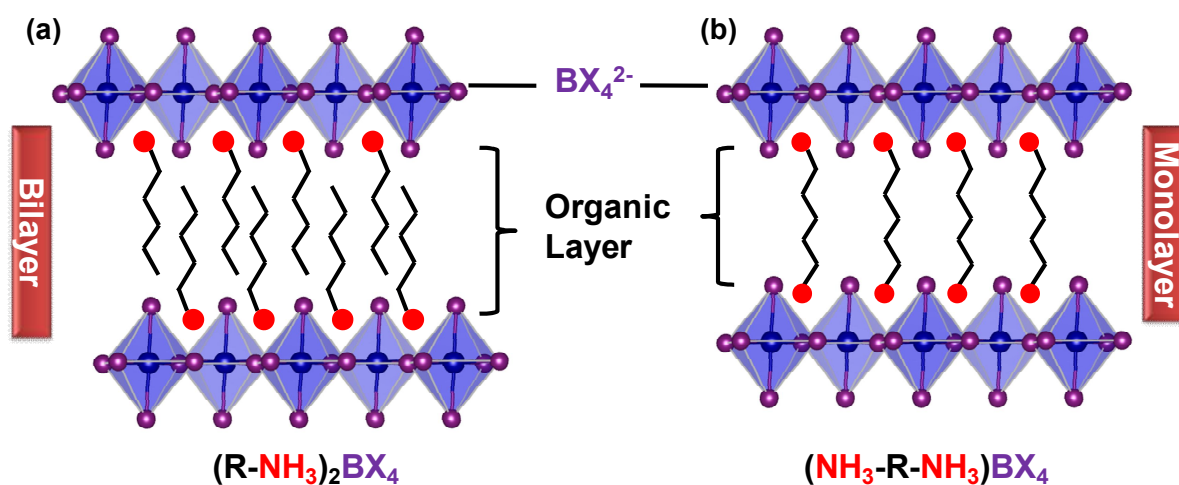


Figure 2. Representation of single layer of <100> orientated hybrid organic inorganic perovskite. (a) Monoammonium organic cation (Ruddlesden-Popper phase) and (b) diammonium organic cation (Dion-Jacobson phase).

Depending on the valency of organic cation, layered perovskites mainly categorized as Ruddlesden-Popper (RP) phase and Dion-Jacobson (DJ) phase. In the RP phase, the organic layer is a bilayer comprised of two monofunctional cations and shifts in inorganic layers w.r.t. each other (Figure 2(a)). However, in the DJ phase, perfectly aligned inorganic layers are separated by the monolayer of bifunctional cations (Figure 2(b)).

Some drawbacks become evident in 3D perovskites (e.g. CH₃NH₃PbI₃), despite astonishing performance in the photovoltaic application reaching the solar cell power conversion efficiency ~25.2%.⁹ One of the significant concern is insufficient devices stability over a long period of time, and other is lead (Pb) toxicity.^{10, 11} Though later problem already been resolved by incorporating environment-friendly element like tin

(Sn) in 3D analogues (e.g. $\text{CH}_3\text{NH}_3\text{SnI}_3$).¹²⁻¹⁶ The earlier problem with stability is not satisfactorily addressed yet. One of the proposed solutions to this problem is replacing the 3D perovskites with the 2D layered perovskite. Because hydrophobic organic cations¹⁷ and van der Waals interactions between the organic molecules¹⁸ make the layered perovskites resistant to moisture compared to their 3D analogues.¹⁹ Also in this system, physical properties, including the band tunability and structural flexibility can be attained with ease.

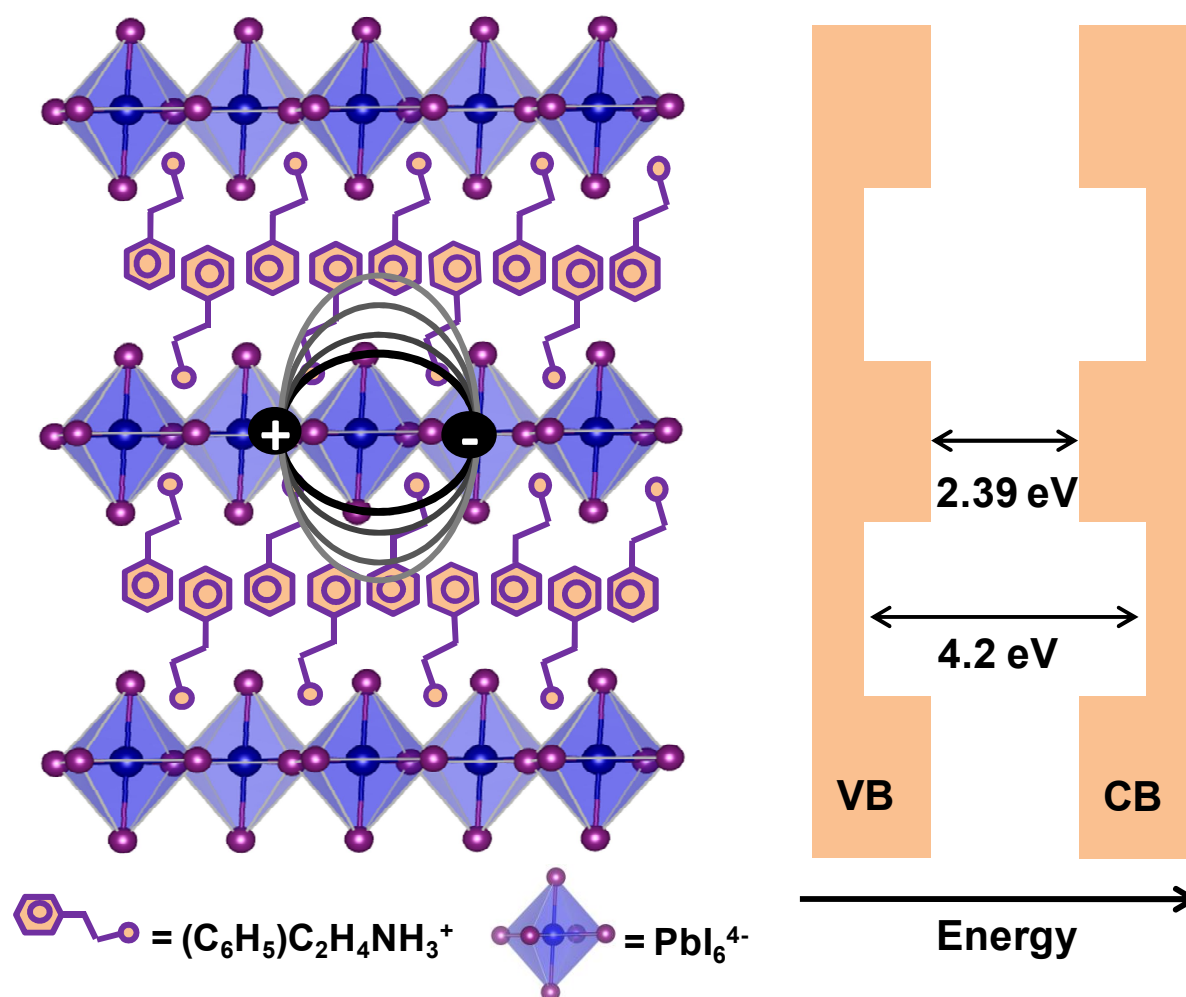


Figure 3. Structure of $(\text{C}_6\text{H}_5)_2\text{C}_2\text{H}_4\text{NH}_3^+_2\text{PbI}_4$ with alternating organic and inorganic layers forming the multiple quantum well (MQW) structures. At the same time, the schematic represents dielectric confinement experienced by the exciton. (“-” and “+” symbols indicate electron and hole respectively which are bound to form an exciton) VB: valence band, CB: conduction band.

Apart from the moisture stability, 2D layered perovskites provide potential benefits. For example, the inorganic framework provides high carrier mobilities and organic

molecules facilitate intense photoluminescence (PL) owing to quantum confinement effect²⁰ and dielectric confinement effect²¹. 2D layered perovskite systems are regarded as natural multiple quantum wells (MQW) in which insulating organic layer act as “barriers” and conducting inorganic layers act as “well”. As shown in Figure 3, 2D perovskite like $((\text{C}_6\text{H}_5)\text{C}_2\text{H}_4\text{NH}_3)_2\text{PbI}_4$ comprised with the alternating inorganic (PbI_6^{4-} octahedra) and organic $((\text{C}_6\text{H}_5)\text{C}_2\text{H}_4\text{NH}_3)^+$ layers forms self assemble MQW structures with thickness 0.6 nm and ~ 1 nm respectively.²² Length of the organic cation (insulating layer thickness) and inorganic layer thickness play a crucial role in controlling the bandgap of the material. An increase in inorganic layer thickness decreases the bandgap.²³ The large dielectric difference between the inorganic layer ($\epsilon_{\text{in}}=6.1$) and an insulating layer ($\epsilon_{\text{org}}= 3.32$) give rise to strong dielectric confinement which further enhances oscillator strength²⁴ and excitonic binding energy²⁵.

The heavy atoms in the 2D HOIP contribute to strong spin-orbit coupling. In the presence of strong spin-orbit coupling and inversion symmetry breaking introduces the spin splitting in continuum band known as “Rashba Splitting”.²⁶ Also 2D HOIP exhibit high charge carrier mobility²⁷, intrinsic multiple quantum well structure, facile solution processability. So these make the 2D HOIP perovskite the potential candidate for the spintronic and optoelectronic applications.^{28, 29} It has been observed that the layered perovskite like $(\text{C}_6\text{H}_5\text{C}_2\text{H}_4\text{NH}_3)_2\text{PbI}_4$ single crystal gives distinct excitonic photoluminescence (PL) peaks at room temperature and low temperature ($<75\text{K}$). Some reports attributed such fine exciton emission features are due to Rashba splitting.^{30, 31} However, the observed difference in emission peak values is ~ 152 meV which is quite large compare to a spin-orbit splitting value (~ 45 meV).

Recently, Sheikh et al. observed the dual excitonic emission features in the series of lead halide based hybrid 2D layered perovskite systems.^{32, 33} Such dual excitonic emission is very unusual, and difficult to explain based on the known 2D electronic structure of this material. This raises the question of whether we understand the electronic and optical properties of hybrid layered metal halide perovskites. To answer this question, we studied a series of Sn-halide hybrid layered perovskites, which are analogous to corresponding Pb-halide systems. Besides spin-orbit splitting values for the Sn are negligible compare to Pb that will also help us to verify any possible contribution of spin-orbit coupling in the dual emission.

In this thesis, we will discuss the synthesis and characterization of the Sn based 2D layered perovskites single crystals of $((\text{C}_6\text{H}_5)\text{C}_2\text{H}_4)_2\text{SnI}_4$, $(\text{C}_4\text{H}_9\text{NH}_3)_2\text{SnI}_4$, $(\text{C}_6\text{H}_{13}\text{NH}_3)_2\text{SnI}_4$, $(\text{C}_8\text{H}_{17}\text{NH}_3)_2\text{SnI}_4$ and $(\text{C}_6\text{H}_{16}\text{N}_2)\text{SnI}_4$.

2. Experimental Section:

2.1 Chemicals:

Hydriodic acid (HI, 57 wt %), stannous oxide (SnO, 97%), lead oxide (PbO, 99.99%), 1-phenylethylamine $((\text{C}_6\text{H}_5)\text{C}_2\text{H}_4\text{NH}_2$, 99%), n-butylamine $(\text{C}_4\text{H}_9\text{NH}_2$, 99%), n-hexylamine $(\text{C}_6\text{H}_{13}\text{NH}_2$, 99%), n-octylamine $(\text{C}_8\text{H}_{17}\text{NH}_2$, 99%), 4-(aminomethyl)piperidine $(\text{C}_6\text{H}_{14}\text{N}_2$, 96%), are purchased from Sigma Aldrich Chemicals. Hypophosphorous acid $(\text{H}_3\text{PO}_2$, 50% w/w H_2O) is purchased from Avra. All chemicals are used without having further purification.

2.2 Synthesis Methods:

2.2.1 Synthesis of $((\text{C}_6\text{H}_5)\text{C}_2\text{H}_4\text{NH}_3)_2\text{SnI}_4$ single crystal:

For the synthesis of $((\text{C}_6\text{H}_5)\text{C}_2\text{H}_4\text{NH}_3)_2\text{SnI}_4$ termed as $(\text{PEA})_2\text{SnI}_4$ single crystals, 80 mg (0.6 mmol) SnO is transferred to 20 ml vial inside N_2 filled glovebox, then vial is tightly sealed with rubber cap. Outside in ambient condition 6 ml of 57% w/w aqueous HI and 3 ml 50% aqueous H_3PO_2 added in vial via syringe. Such a mixture is heated to 100°C with vigorous stirring until a clear light yellow solution is observed. After 30 minutes, 0.16 ml (1.2 mmol) of $(\text{C}_6\text{H}_5)\text{C}_2\text{H}_4\text{NH}_2$ is added to the above mixture and stirring stopped after the solution becomes clear. Then the solution is allowed to cool down to room temperature. This method yields centimetre sized brown plate-like crystals which were filtered, dried, and used for the further characterization.

2.2.2 Synthesis of $(\text{C}_4\text{H}_9\text{NH}_3)_2\text{SnI}_4$ single crystal:

For the synthesis of $(\text{C}_4\text{H}_9\text{NH}_3)_2\text{SnI}_4$, i.e. $(\text{BA})_2\text{SnI}_4$ single crystals, 168 mg (1.25 mmol) of SnO is transferred to 20 ml vial inside N_2 filled glovebox, then vial is tightly sealed with rubber cap. Outside in ambient condition 5 ml of 57% w/w aqueous HI and 3 ml 50% aqueous H_3PO_2 added in vial via syringe. Such a mixture is heated to 90°C with vigorous stirring until a clear light yellow solution is observed. After 30 minutes, 0.25 ml (2.5 mmol) of $\text{C}_4\text{H}_9\text{NH}_2$ is added to the above mixture, and stirring

stopped after the solution becomes clear. During the cooling process, brown plate-like crystals observed. Crystals were removed from vial carefully, dried, and used for further characterization.

2.2.3 Synthesis of $(C_6H_{13}NH_3)_2SnI_4$ single crystal:

$(C_6H_{13}NH_3)_2SnI_4$, termed as $(HA)_2SnI_4$ single crystals, 68 mg (0.5 mmol) of SnO is transferred to 20 ml vial inside N_2 filled glovebox, then vial is tightly sealed with a rubber cap. Outside in ambient condition 5 ml of 57% w/w aqueous HI and 3 ml 50% aqueous H_3PO_2 added in vial via syringe. Such a mixture is heated to $90\text{ }^\circ\text{C}$ with vigorous stirring for 30 minutes until a clear light yellow solution is observed. 0.13 ml (1 mmol) of $C_6H_{13}NH_2$ is added to the above mixture, and after the appearance of a clear solution, stirring stopped. Then the solution is allowed to cool down to room temperature. This method yields millimetre sized brown plate-like crystals which were removed from vial carefully, dried, and used for further characterization.

2.2.4 Synthesis of $(C_8H_{17}NH_3)_2SnI_4$ single crystal:

For the synthesis of $(C_8H_{17}NH_3)_2SnI_4$, i.e. $(OA)_2SnI_4$ single crystals, 34 mg (0.25 mmol) of SnO is transferred to 20 ml vial inside N_2 filled glovebox, and then vial is tightly sealed with rubber cap. Outside in ambient condition 5 ml of 57% w/w aqueous HI and 3 ml 50% aqueous H_3PO_2 added in vial via syringe. Such a mixture is heated to $140\text{ }^\circ\text{C}$ with vigorous stirring until a clear light-yellow solution is observed. 0.08 ml (0.5 mmol) $C_8H_{17}NH_2$ is added to the above mixture, and after a clear solution, stirring quickly stopped. Then the solution is allowed to cool down to room temperature. This method yields brown plate-like crystals which were filtered, dried, and used for further characterization.

2.2.5 Synthesis of $(C_6H_{16}N_2)SnI_4$ single crystal:

For the synthesis of $(C_6H_{16}N_2)SnI_4$, i.e. 4-AMPSnI₄ single crystals, 135 mg (1 mmol) of SnO is transferred to 20 ml vial inside N_2 filled glovebox, then vial is tightly sealed with rubber cap. Outside in ambient condition 6 ml of 57% w/w aqueous HI and 3 ml 50% aqueous H_3PO_2 added in vial via syringe. Such a mixture is heated to $160\text{ }^\circ\text{C}$ with vigorous stirring until a clear light-yellow solution is observed. 0.08 ml (1 mmol) of $C_6H_{14}N_2$ is added to the above mixture with vigorous stirring. During the cooling

process, dark brown crystals were observed. Crystals were filtered, dried, and used for further characterization.

2.2.6 Synthesis of (C₆H₁₆N₂)PbI₄ single crystal:

For the synthesis of (C₆H₁₆N₂)PbI₄ termed as 4-AMPPbI₄ single crystals, 223 mg (1 mmol) of PbO is transferred to 20 ml vial inside N₂ filled glovebox, and then vial is tightly sealed with rubber cap. Outside in ambient condition 57% w/w aqueous HI and 3 ml 50% aqueous H₃PO₂ added in vial via syringe. Such a mixture is heated to 190 °C with vigorous stirring until a clear light yellow solution is observed. 0.08 ml (1 mmol) of C₆H₁₄N₂ is added to the above mixture with vigorous stirring until the solution becomes transparent. Then the solution is allowed to cool down to room temperature. This method yields dark brown crystals that were filtered, dried and used for further characterization.

2.2.7 Exfoliated (PEA)₂SnI₄, (BA)₂SnI₄, (HA)₂SnI₄ and (OA)₂SnI₄:

By the scotch-tape method, exfoliated samples were prepared for further studies. A single crystal with dimensions ~(2 x 2 x 0.2) mm was stuck on scotch tape and exfoliated by separating apart the layers in the single crystal with the help of scotch tape.

2.3 Characterization Techniques:

2.3.1 Single crystal X-ray diffraction (SCXRD): Full sphere diffraction data were collected using Bruker Apex Duo Diffractometer at 100 K and 298 K using K α radiation of Mo (λ = 0.71073 Å) and Cu (λ = 1.54178 Å). A single crystal was selected and kept under an N₂ atmosphere during the whole measurement. Using the APEX3 software, the collected data were integrated and applied with numerical absorption corrections. The structures were solved by direct method and refined by full-matrix least-squares on F² using the SHELXTL software package. The PbI₄ and SnI₄ framework was refined anisotropically. All organic atoms were refined isotropically, and C–C and C–N bond lengths were restrained to ideal values.

2.3.2 Powder X-ray diffraction (PXRD): PXRD patterns were collected with a Bruker D8 Advance X-ray diffractometer using Cu K α radiation (λ = 1.54178 Å). A single flake of crystal is picked for the PXRD data collection.

2.3.3 UV-vis absorption spectroscopy: Transmission mode UV-visible absorption spectra of thin flake single crystals and exfoliated single crystals measured using a Cary series UV visible spectrophotometer.

2.3.4 UV-vis-NIR diffused reflectance spectroscopy: A Shimadzu UV-3600 plus UV-vis-NIR spectrophotometer is used for diffused reflectance spectra measurement of single crystal samples in 200-800 nm region using BaSO₄ as a reference of 100% reflectance.

2.3.5 Steady-state photoluminescence (PL) spectroscopy and PL decay dynamics: Steady-state photoluminescence (PL) spectra and PL decay dynamics (TCSPC, time-correlated single photon counting) are recorded using FLS 980 spectrophotometer (Edinburgh Instruments). Picosecond pulsed diode laser (405 nm) is used as an excitation source for excitonic PL decay dynamics.

2.3.6 Scanning electron microscopy (SEM): Imaging of crystal flakes is carried out using a Zeiss Ultra Plus field emission SEM instrument.

2.3.7 Atomic force microscopy (AFM): AFM data were collected in the tapping mode technique using the Keysight atomic force microscope (model: AFM 5500).

3. Results and Discussion

3.1 Characterisation of (PEA)₂SnI₄ single crystal:

Here we followed the novel synthesis method for (PEA)₂SnI₄ single crystals as mentioned in experimental section 2.2.1. This leads to centimetre size layered single crystal flakes as shown in Figure 4(a-b). In the PXRD pattern (Figure 4(c)), we observed periodic diffraction peaks corresponding to interlayer spacing. Since preferred crystal growth is along the one particular direction responsible for such periodic diffraction intensities in PXRD. As per Bragg's formula $2d\sin\theta = n\lambda$, calculated inorganic interlayer separation distance (d) is 16.4 Å which corresponds to the stacking of phenyl rings. Besides, no peaks correspond to other phases (e.g. 1D or 0D) observed that clearly implies phase pure synthesis. Figure 4(d) represents solved single crystal structure for (PEA)₂SnI₄ at 298 K. (PEA)₂SnI₄ crystallizes in triclinic crystal structure with space group P -1 and lattice parameters $a = 8.805 \text{ \AA}$, $b = 8.83 \text{ \AA}$, $c = 16.99 \text{ \AA}$ with d spacing 16.99 Å which is closer to 16.4 Å. Overall phase pure synthesis of (PEA)₂SnI₄ is confirmed from PXRD and SCXRD.

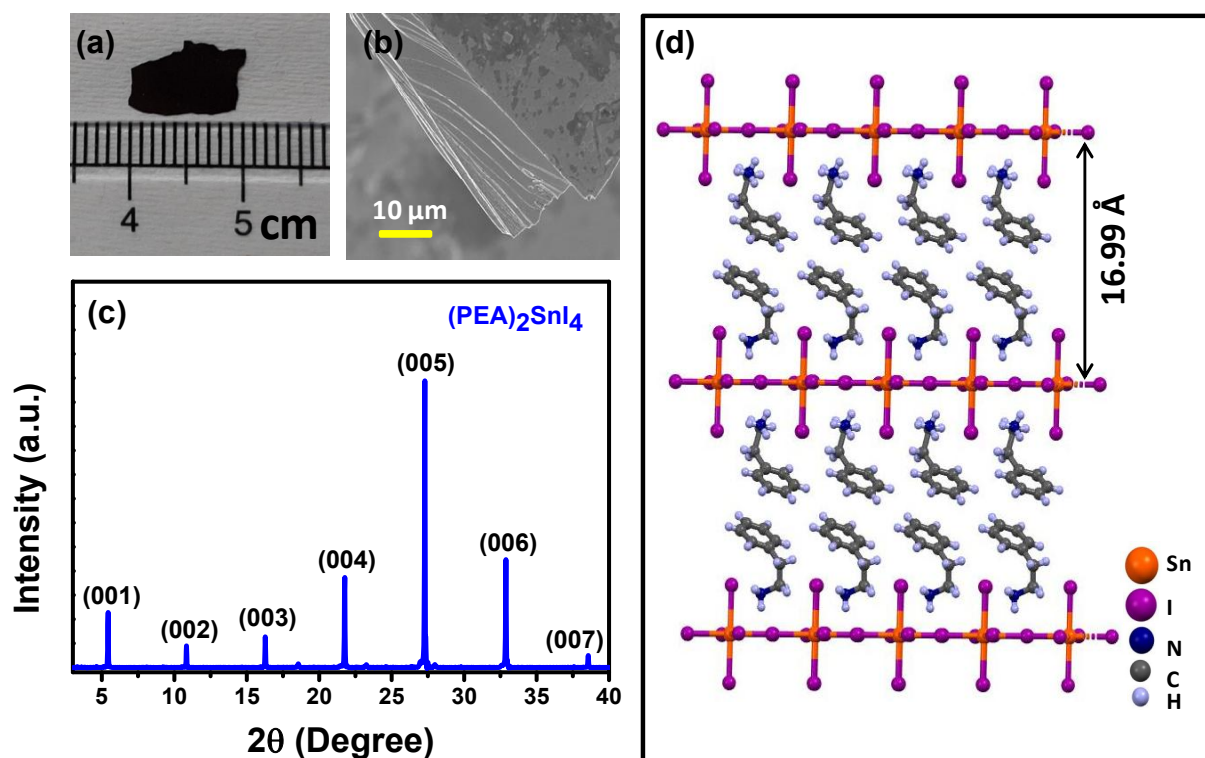


Figure 4. Morphology and structural characterization of $(\text{PEA})_2\text{SnI}_4$. (a) Digital photograph of centimetre size single crystal flake, (b) SEM image at the edge of the crystal, (c) PXRD pattern of the single crystal and (d) ball and stick model of $(\text{PEA})_2\text{SnI}_4$ which was obtained on solving SCXRD recorded at 298 K.

Table 1. Crystal data and structure refinement for $(\text{PEA})_2\text{SnI}_4$.^a

Identification code	PEASI_RT	
Chemical formula	$\text{C}_{16}\text{H}_{24}\text{I}_4\text{N}_2\text{Sn}$	
Formula weight	870.66 g/mol	
Temperature	296(2) K	
Wavelength	0.71073 Å	
Crystal system	triclinic	
Space group	$P-1$	
Unit cell dimensions	$a = 8.805(13)$ Å	$\alpha = 85.14(6)^\circ$
	$b = 8.83(2)$ Å	$\beta = 80.23(4)^\circ$
	$c = 16.99(3)$ Å	$\gamma = 90.01(8)^\circ$
Volume	$1297(4)$ Å ³	
Z	2	
Density (calculated)	2.229 g/cm ³	
Absorption coefficient	5.745 mm ⁻¹	
F(000)	792	
Independent reflections	7942 [R (int) = 0.0607]	
Data / restraints / parameters	7942 / 7 / 189	

Goodness-of-fit on F^2	1.168
Δ/σ_{\max}	2.385
Final R indices [$l > 2\sigma(l)$]	$R_1 = 0.0664$, $wR_2 = 0.1782$
R indices [all data]	$R_1 = 0.1136$, $wR_2 = 0.2007$
Largest diff. peak and hole	3.594 and -1.554 e\AA^{-3}

^a $R = \sum ||F_o| - |F_c|| / \sum |F_o|$, $wR = \{ \sum [w(|F_o|^2 - |F_c|^2)^2] / \sum [w(|F_o|^4)] \}^{1/2}$ and $w = 1/(\sigma^2(l) + 0.1000P^2)$, $P = (F_o^2 + 2F_c^2)/3$.

3.2 Photophysical study of $(\text{PEA})_2\text{SnI}_4$ single crystal:

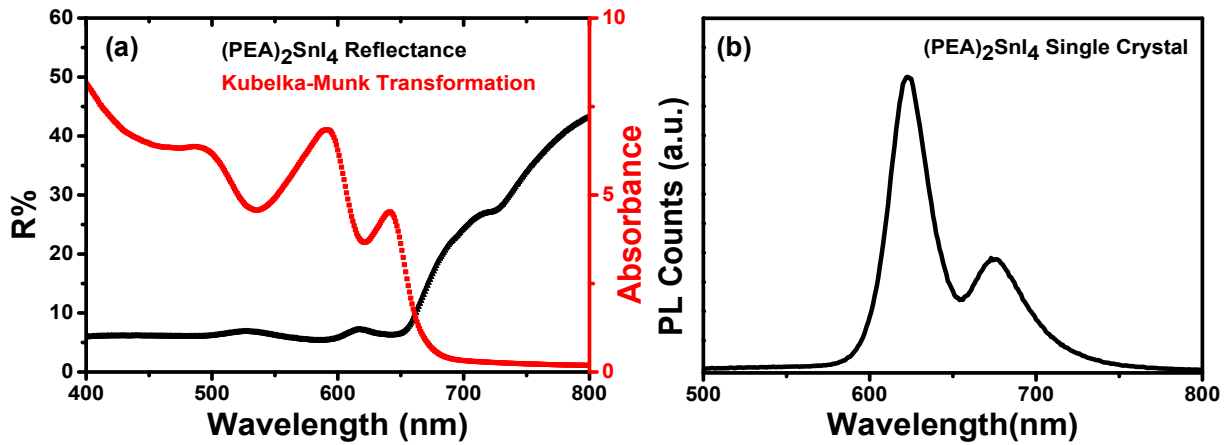


Figure 5. Photophysical study of $(\text{PEA})_2\text{SnI}_4$ single crystals. (a) Recorded reflectance spectrum (black) and corresponding Kubelka-Munk transformation to absorbance spectrum (red). (b) PL spectrum recorded with excitation at 405 nm.

Figure 5(a) shows the reflectance spectrum (black line) of single crystals of $(\text{PEA})_2\text{SnI}_4$ and corresponding Kubelka-Munk transformation to the absorption spectrum (red line). We observed the lowest energy absorption peak at 641 nm. In PL setup, the angle between the sample, excitation source and detector is 45° . As the surface of the sample gets excited, the coming out emission is collected by placing a detector on the same front side of the sample. PL is recorded from the front side of the crystal flake give rise to distinct emission peaks at 625 nm and 680 nm, as shown in Figure 5(b). It is to be noted here that the PL peak at 625 nm is at higher energy (lower wavelength) compared to the lowest energy absorption peak at 641 nm. This is very unusual.

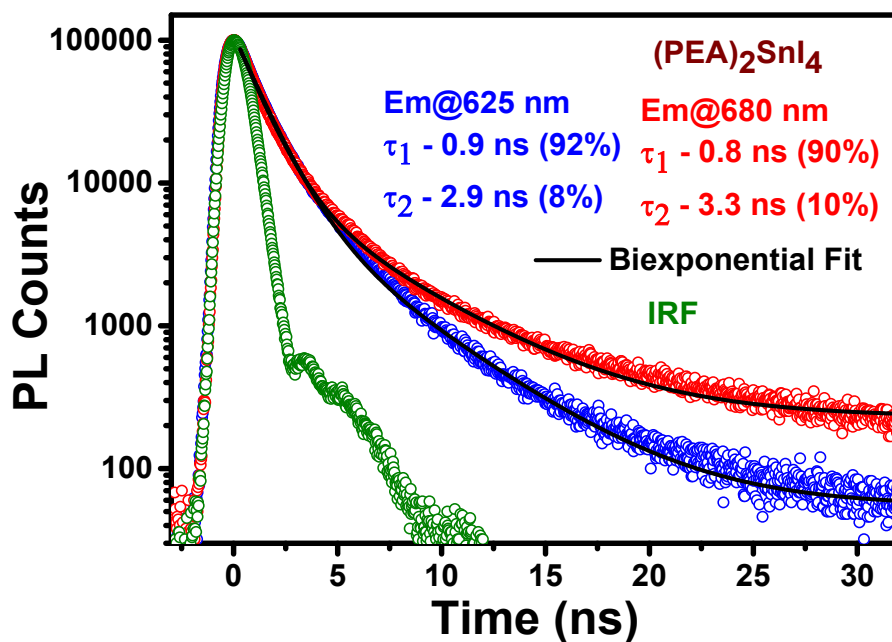


Figure 6. PL decay dynamics recorded at 625 nm (blue) and 680 nm (red) for $(\text{PEA})_2\text{SnI}_4$ with excitation at 405 nm.

PL decay dynamics data confirms that both the 625 nm and 680 nm PL features have similar nanosecond scale lifetime (Figure 6). Such shorter lifetime indicates that both emissions are due to excitonic transition with strong recombination probabilities. The difference between the two emission peaks in $(\text{PEA})_2\text{SnI}_4$ is 160 meV which is comparable to 152 meV observed in $(\text{C}_6\text{H}_5\text{C}_2\text{H}_4\text{NH}_3)_2\text{PbI}_4$, i.e. $(\text{PEA})_2\text{PbI}_4$.

3.3 Exfoliated $(\text{PEA})_2\text{SnI}_4$:

The single crystals are exfoliated mechanically using the standard scotch tape technique. AFM image in Figure 7(a) and corresponding height profile in Figure 7(b) shows ~ 80 nm thick exfoliated sample. On exfoliation absorption edge shifts towards the high energy (Figure 7(c)). Also, the PL spectrum shows a single broad peak at 634 nm in Figure 7(d). The difference in optical absorption and PL spectra exfoliated sample with that of single crystals might arise because of inhomogeneity in exfoliated samples and/or intrinsic differences in the interlayer interactions in both kinds of samples. Further study is required to understand these results.

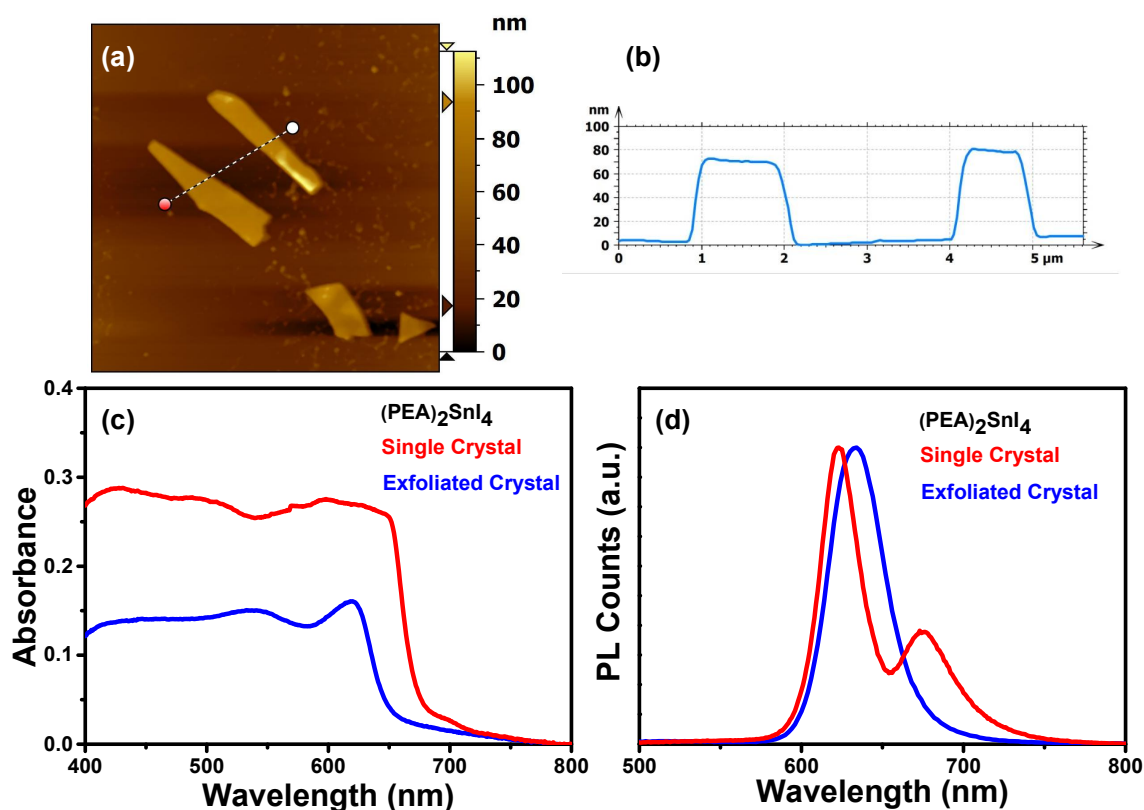


Figure 7. Exfoliated $(\text{PEA})_2\text{SnI}_4$. (a) AFM image and (b) height profile across the dotted line on the AFM image in (a). (c) UV-visible absorbance (transmission mode) spectra recorded on single crystal (red) and exfoliated crystals (blue). (d) PL spectra measured on single crystal (red) and exfoliated crystals (blue) with excitation at 405 nm.

3.4 Characterisation of $(\text{BA})_2\text{SnI}_4$, $(\text{HA})_2\text{SnI}_4$ and $(\text{OA})_2\text{SnI}_4$ single crystals:

Above observation raises the question, do other Sn-iodide RP perovskites show the dual excitonic features similar to $(\text{PEA})_2\text{SnI}_4$? Does dual excitonic emission property depend on the organic layer?

To tackle the above questions, we have synthesized the Sn-iodide RP perovskites such as $(\text{BA})_2\text{SnI}_4$, $(\text{HA})_2\text{SnI}_4$ and $(\text{OA})_2\text{SnI}_4$ as per above mentioned methods. So far, all the synthesized layered perovskite single crystals take the flakes like shape where one dimension is very less compared to the other two. That results in dominant periodic diffraction peaks along (00l) planes. The periodic arrangement of diffraction peaks in PXRD (Figure 8(a)) and distinct layers in SEM images (Figure 8(b-d)) confirms phase pure synthesis of 2D layered $(\text{BA})_2\text{SnI}_4$, $(\text{HA})_2\text{SnI}_4$ and $(\text{OA})_2\text{SnI}_4$.

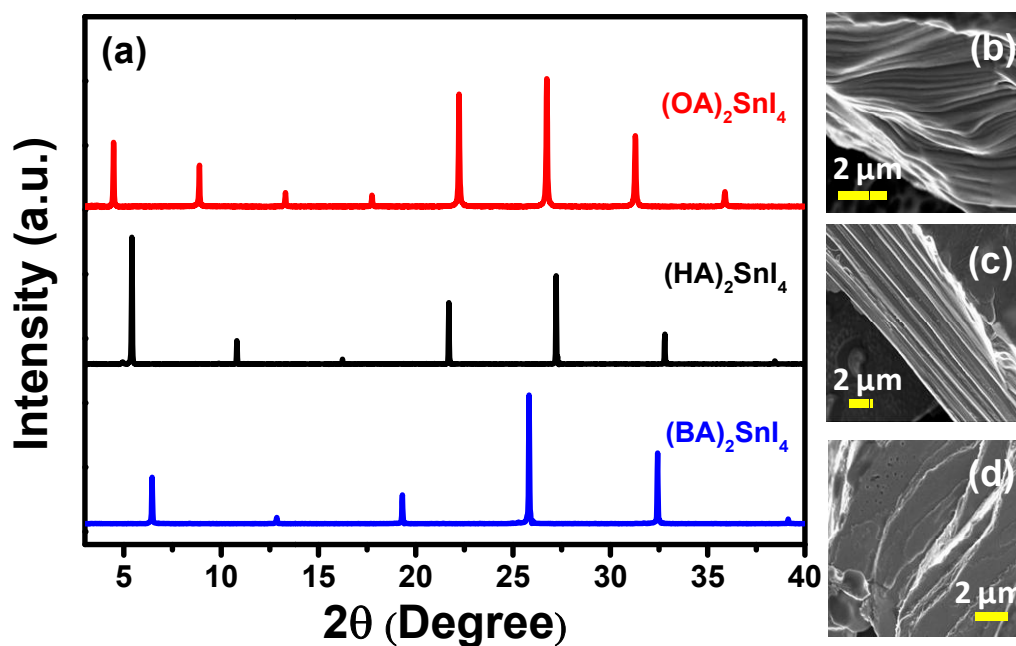


Figure 8. Structural characterization of $(\text{BA})_2\text{SnI}_4$, $(\text{HA})_2\text{SnI}_4$ and $(\text{OA})_2\text{SnI}_4$. (a) PXRD recorded for single crystals of $(\text{BA})_2\text{SnI}_4$ (blue), $(\text{HA})_2\text{SnI}_4$ (black) and $(\text{OA})_2\text{SnI}_4$ (red) at room temperature. SEM images shows the morphology of $(\text{BA})_2\text{SnI}_4$ (b), $(\text{HA})_2\text{SnI}_4$ (c) and $(\text{OA})_2\text{SnI}_4$ (d).

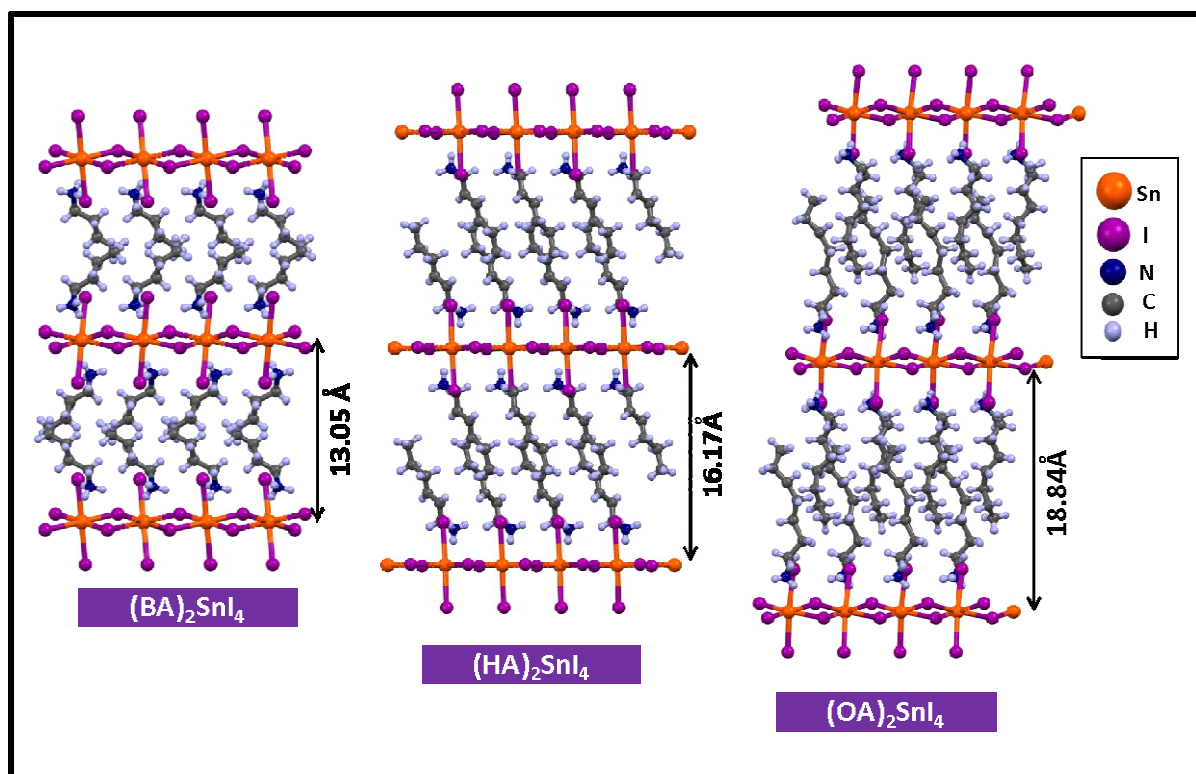


Figure 9. Ball and stick representation of $(\text{BA})_2\text{SnI}_4$, $(\text{HA})_2\text{SnI}_4$ and $(\text{OA})_2\text{SnI}_4$ obtained from SCXRD data collected at 100 K.

Table 2. Crystal data and structure refinement for (BA)₂SnI₄, (HA)₂SnI₄ and (OA)₂SnI₄.^a

Identification code	BASI_100K	HASI_100K	OASI_100K
Chemical formula	C ₈ H ₂₄ I ₄ N ₂ Sn	C ₁₂ H ₃₂ I ₄ N ₂ Sn	C ₁₆ H ₄₀ I ₄ N ₂ Sn
Formula weight	774.62 g/mol	830.68 g/mol	886.79 g/mol
Temperature	100(2) K	100(2) K	100(2) K
Wavelength	1.54178 Å	0.71073 Å	0.71073 Å
Crystal system	monoclinic	monoclinic	monoclinic
Space group	P2(1)/c	P 1 2 ₁ /c 1	P 1 c 1
Unit cell dimensions	a = 26.105(6) Å	a = 16.167(7) Å	a = 18.836(19) Å
	b = 8.944(3) Å	b = 8.807(4) Å	b = 9.061(9) Å
	c = 8.398(2) Å	c = 8.582(4) Å	c = 8.411(9) Å
	β = 90.215(15)°	β = 91.914(13)°	β = 97.44(2)°
Volume	1960.8(9) Å ³	1221.2(9) Å ³	1423.(2) Å ³
Z	4	2	4
Density (calculated)	2.617 g/cm ³	2.259 g/cm ³	4.138 g/cm ³
Absorption coefficient	59.666 mm ⁻¹	6.097 mm ⁻¹	10.475 mm ⁻¹
F(000)	1384	760	1648
Independent reflections	2937 [R (int) = 0.1115]	3052 [R (int) = 0.0976]	1678 [R (int) = 0.0659]
Data / restraints / parameters	2937 / 4 / 143	3052 / 4 / 90	1678 / 22 / 212
Goodness-of-fit on F ²	1.947	4.003	3.094
Δ/σmax	1.329	0.529	4.175
Final R indices [I > 2σ(I)]	R ₁ =0.1563, wR ₂ =0.3499	R ₁ =0.2147, wR ₂ =0.5320	R ₁ =0.1554, wR ₂ =0.3941
R indices [all data]	R ₁ =0.1983, wR ₂ =0.3620	R ₁ =0.2242, wR ₂ =0.5341	R ₁ =0.1696, wR ₂ =0.4128
Largest diff. peak and hole	4.429 and -3.859 eÅ ⁻³	17.012 and -8.708 eÅ ⁻³	7.097 and -3.803 eÅ ⁻³

^a $R = \frac{\sum ||F_o| - |F_c||}{\sum |F_o|}$, $wR = \left\{ \frac{\sum [w(|F_o|^2 - |F_c|^2)^2]}{\sum [w(|F_o|^4)]} \right\}^{1/2}$ and $w = 1/(\sigma^2(I) + 0.1000P^2)$, $P = (F_o^2 + 2F_c^2)/3$.

At the same time, no other diffraction intensities were present corresponding to other plausible dimensional phases such as 1D or 0D.

From Bragg's formula $2d\sin\theta = n\lambda$, calculated d spacing corresponds to the inorganic interlayer distance for (BA)₂SnI₄, (HA)₂SnI₄ and (OA)₂SnI₄ are 13.5 Å, 16.0 Å and 19.7 Å respectively. Single crystal X-ray diffraction data further provide evidence for

the formation of 2D layered $(\text{BA})_2\text{SnI}_4$, $(\text{HA})_2\text{SnI}_4$ and $(\text{OA})_2\text{SnI}_4$ perovskites with an interlayer spacing of 13.05 Å, 16.17 Å and 18.84 Å respectively (Figure 9). All the three samples have a monoclinic crystal system with similar 'b' and 'c' lattice parameters since all of them have similar inorganic framework extended in the plane. However, the change in 'a' is observed due to the different length of the organic cation (Table 2). Going from BA, HA to OA, we find the systematic increase in interlayer spacing with an increase in carbon chain length of the organic cation. The lower interlayer spacing distance in SCXRD compared to PXRD is attributed to a decrease in bond distances at 100 K.

During the single crystal XRD measurements, we observed that if we mount sample for a longer time, then degradation or deformation of sample is inevitable. So here we suggest recording reflection frames as quick as possible (~0.8 s/frame) at a lower temperature (~100 K).

3.5 Photophysical study of $(\text{BA})_2\text{SnI}_4$, $(\text{HA})_2\text{SnI}_4$ and $(\text{OA})_2\text{SnI}_4$ single crystals:

For further photophysical measurements, all samples were kept undisturbed in a vial with reaction solvents. Whenever we desire to record absorbance or PL for samples, we dried the sample on filter paper and then used it for measurement. In this way, even air sensitive Sn perovskite samples can be stored at ambient condition over months without any signs of degradation.

As shown in Figure 10(a), reflectance spectra (dash-dot line) are collected on $(\text{BA})_2\text{SnI}_4$ (C4), $(\text{HA})_2\text{SnI}_4$ (C6) and $(\text{OA})_2\text{SnI}_4$ (C8) single crystals which were converted to absorbance (solid line) via Kubelka-Munk transformation. From absorbance data, excitonic peak values for C4, C6 and C8 are 639 nm, 638 nm and 622 nm respectively. For the C8, significantly different excitonic peak value compared to the other two samples is attributed to tilting of Sn-I octahedra in the crystal structure. Here we can see organic cations control the orientation of semiconducting inorganic layers, which further dictate the optical properties of a material. For all three samples, we measured the PL spectra on a single crystal flake with excitation at 405 nm, as shown in Figure 10(b).

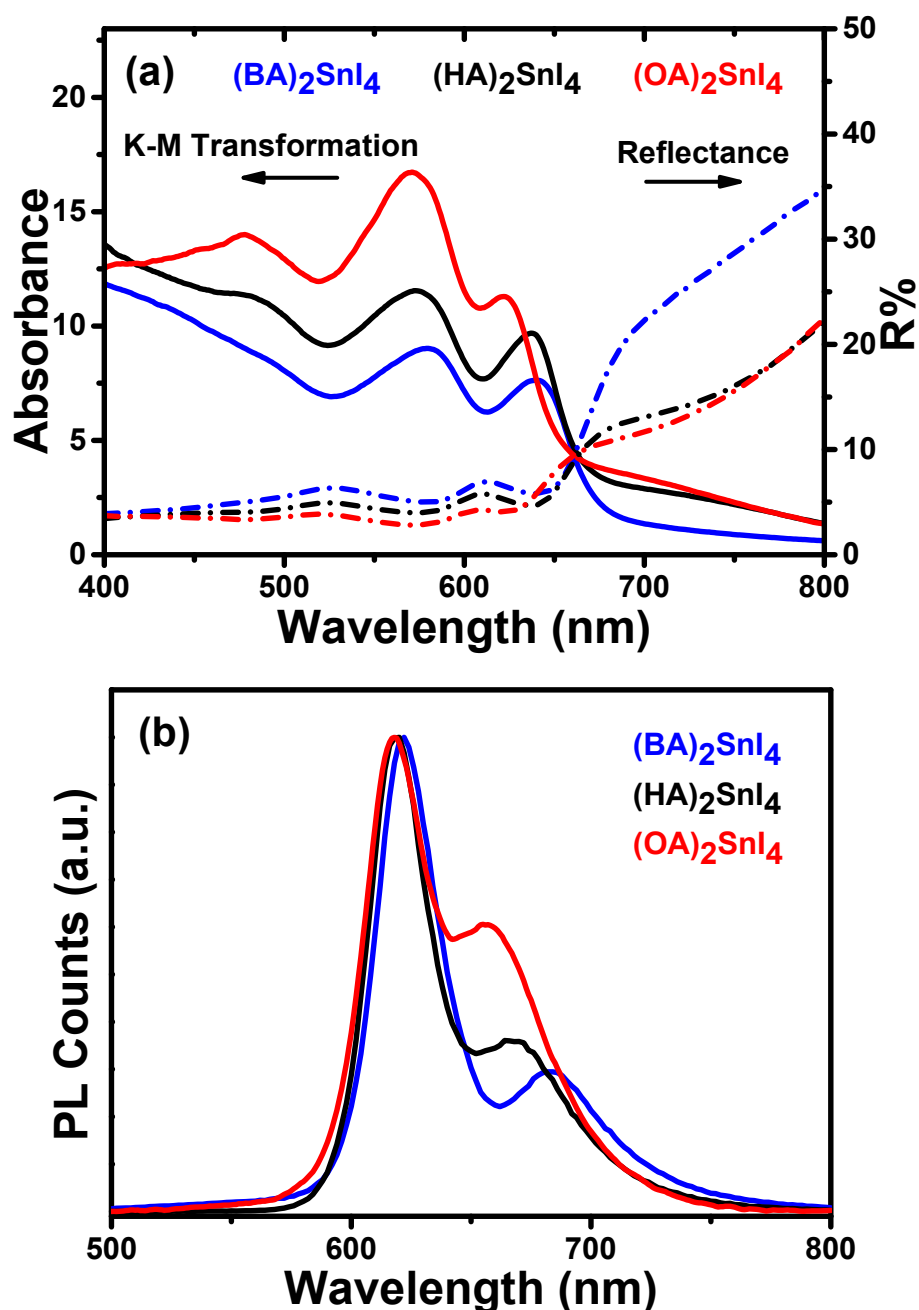


Figure 10. Sample compositions are (BA)₂SnI₄ (blue), (HA)₂SnI₄ (black), and (OA)₂SnI₄ (red). (a) Reflectance spectra (dash-dot lines) and corresponding Kubelka-Munk transformation to absorbance spectra (solid line) of single crystals. (b) PL spectra of a single crystal flake of the corresponding samples with excitation at 405 nm.

Similar to our previous (PEA)₂SnI₄ system, dual excitonic emission is observed for C4, C6 and C8 systems as well. Different orientation of organic molecules at the edges of crystals compared to the bulk of crystal might be responsible for such dual emission features. In all three systems, high energy emission is observed at ~620

nm, which is independent of organic cation, Figure 10(b). The lower energy emission might originate from possible interlayer interactions near the edges. So when we move from C4 to C8, the interlayer separation between the inorganic layers increases, resulting in a blue-shift in the low energy PL peak. In this way, interlayer interactions can be manipulated through a change in the thickness of the organic layer (insulating layer).

PL decay dynamics data for $(\text{BA})_2\text{SnI}_4$, $(\text{HA})_2\text{SnI}_4$ and $(\text{OA})_2\text{SnI}_4$ show both the peaks have similar few nanosecond lifetimes (Figure 11). The shorter lifetime implies both emissions are due to excitonic transitions with stronger recombination probability. In Sn analogues of Pb, Sheikh et al. already proposed the presence of dual excitonic emission in $(\text{BA})_2\text{PbI}_4$, $(\text{HA})_2\text{PbI}_4$ and $(\text{OA})_2\text{PbI}_4$ systems.^{32, 33}

There can be a small possibility that dual peak emission in layered halide organic inorganic perovskite single crystal is arising due to spin-orbit splitting that depends on the presence of heavy metal atom and inversion symmetry breaking. But our data clearly shows spin-orbit splitting is not responsible for the observed dual emission. Spin-orbit coupling for Sn is very weak compared to that of Pb. However, dual emission peak differences for the analogous Sn-iodide and Pb-iodide systems are comparable (Table 3). Clearly, spin-orbit splitting is not responsible for the observed dual excitonic emission in the above mentioned systems. In $(\text{PEA})_2\text{PbI}_4$ strongest spin-orbit splitting of 45 meV^{30, 31} was observed, which is significantly small compared to 152 meV separation between the two PL peaks. This observation again suggests that the spin-orbit splitting does not give a plausible explanation for our dual excitonic emission.

Dual excitonic emission property is not depending on organic cation in RP perovskite. Similar emission property is observed for $(\text{PEA})_2\text{SnI}_4$, $(\text{BA})_2\text{SnI}_4$, $(\text{HA})_2\text{SnI}_4$ and $(\text{OA})_2\text{SnI}_4$. In all these samples, there is no major change in the inorganic framework. The second point here is that the dual excitonic emission is independent of metal cations. Both Sn or Pb based samples show dual emission, confirming the insignificant role of spin-orbital splitting in the observed dual emission. Overall, the dual excitonic emission is found to be a generic property of 2D hybrid perovskite single crystals with RP phase.

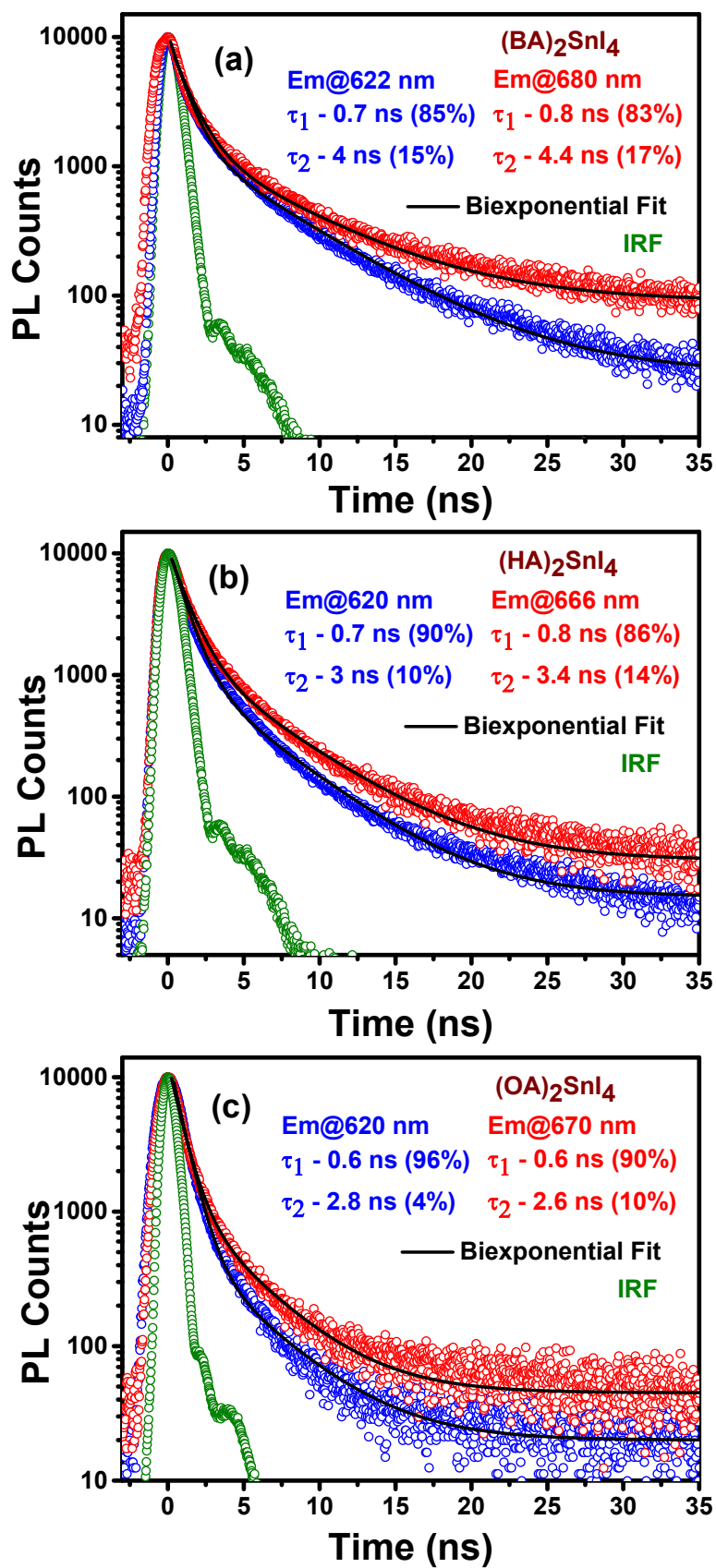


Figure 11. PL decay dynamics measured at both emission peaks of $(\text{BA})_2\text{SnI}_4$ (a), $(\text{HA})_2\text{SnI}_4$ (b) and $(\text{OA})_2\text{SnI}_4$ (c) with excitation of 405 nm.

Table 3. Comparison of dual excitonic emissions for Sn and Pb RP perovskite systems.

System	Emission Peaks (nm)		Peak Difference (meV)	System	Emission Peaks (nm)		Peak Difference (meV)
(PEA) ₂ SnI ₄	625	680	160	(PEA) ₂ PbI ₄	524	560	152
(BA) ₂ SnI ₄	621	680	173	(BA) ₂ PbI ₄	524	560	152
(HA) ₂ SnI ₄	620	666	138	(HA) ₂ PbI ₄	524	558	144
(OA) ₂ SnI ₄	618	656	116	(OA) ₂ PbI ₄	524	550	112

Values for Pb samples were taken from Sheikh et al. ^{32, 33}

3.6 Characterization of 4-AMPPbI₄ single crystals:

What we have understood so far is that dual excitonic emission is the intrinsic property of 2D layered RP perovskite single crystal. As per our previous knowledge the photophysical properties of layered perovskite are mainly dictated by the composition of the inorganic framework since it makes up the valence band and conduction band. On the other hand, organic molecules that separating inorganic layers indirectly affect the photophysical properties. Previous studies done by Sheikh et al. showed phase changes in layered perovskite are associated with the change in the arrangement of organic cations.^{32, 33} Such structural changes results into a change in photophysical properties.

This point raises the next question, will dual emission property be retained even if there is a change in inorganic layer arrangement? To get the answer to this question, we chose a system from the DJ phase mainly because of the following aspects: (i) Instead of two monovalent R-NH₃⁺ ions in RP phase DJ consists of single (NH₃-R-NH₃)²⁺ in the insulating layer; (ii) inorganic layers perfectly aligned on top of each other. In the RP phase, there is a shift in inorganic layer w.r.t. each other. See Figure 2 for a clear comparison of the DJ and RP phase.

For further studies, we successfully synthesized the 4-AMPPbI₄, i.e. (C₆H₁₆N₂)PbI₄ and 4-AMPSnI₄, i.e. (C₆H₁₆N₂)SnI₄ crystals.

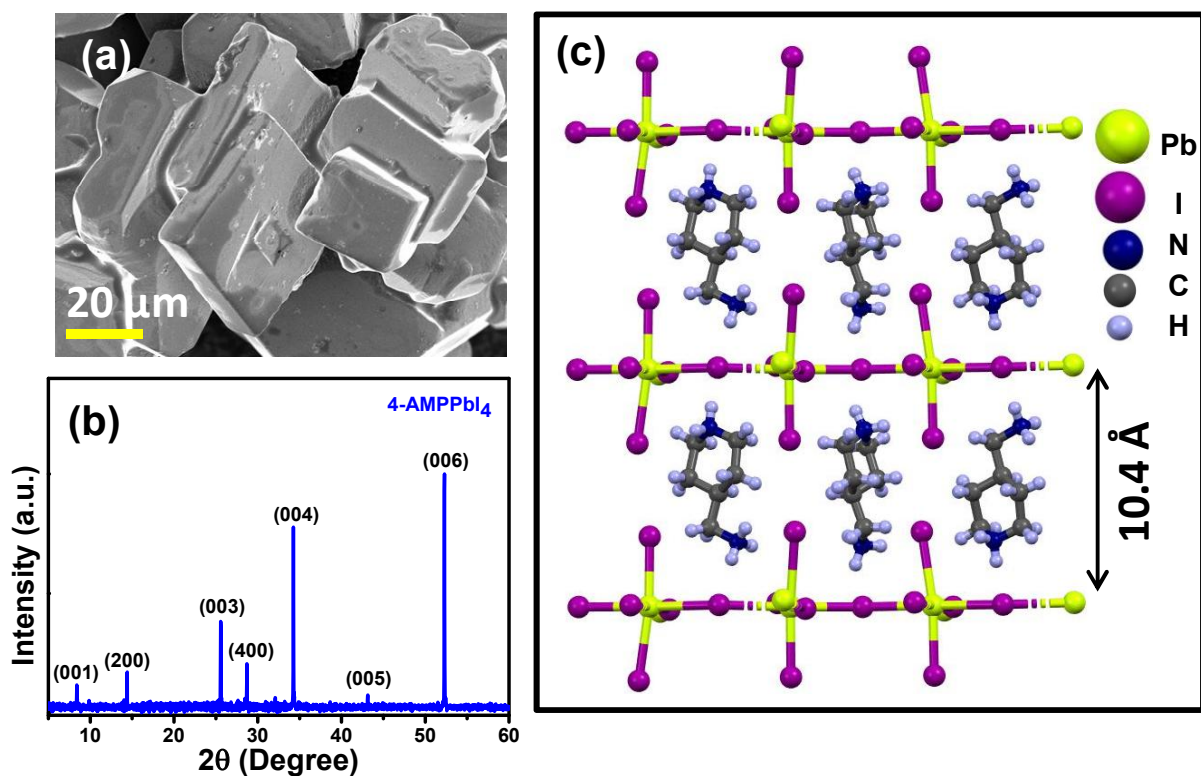


Figure 12. Morphology and structural characterization 4-AMPPbI₄. (a) FESEM image of the 4-AMPPbI₄ sample. (b) PXRD pattern for 4-AMPPbI₄ crystals and (c) solved SCXRD data for 4-AMPPbI₄ recorded at 100 K.

Earlier in the case of (PEA)₂SnI₄ (RP phase), we observed the layered sheet-like structures in the FESEM image (Figure 4(b)). Because in the RP phase, the insulating layer consists of two organic cations interacting with each other via weak van der Waals forces. Due to this reason crystal gets easily cleaved along the planes with weak van der Waals interactions. Here, we successfully synthesized the DJ phase 4-AMPPbI₄ microcrystals (~50 μm), as shown in Figure 12(a). In the case of 4-AMPPbI₄, there is only a single cation separating the two inorganic layers, so it is difficult to cleave the crystal. That's why instead of the sheet-like morphology, we observe the cuboidal crystal in the FESEM image.

Even though there are some morphological differences between the RP and DJ phase, both systems exhibit layered structure with 2D electronic confinement. Therefore, PXRD data of 4-AMPPbI₄ are dominated by the (00l) planes that result in periodic diffraction peaks (Figure 12(b)), similar to RP phase. The calculated d spacing using Bragg's formula is 10.4 Å, which perfectly matches with the distance

between the PbI_4^{2-} layers separated by 4-AMP (4-amino(methyl)piperidine) cations (Figure 12(c)).

Table 4. Crystal data and structure refinement for 4-AMPPbI₄.^a

Identification code	4-AMPPbI4_100K
Chemical formula	C ₆ H ₁₆ I ₄ N ₂ Pb
Formula weight	831.00 g/mol
Temperature	100(2) K
Wavelength	1.54178 Å
Crystal system	orthorhombic
Space group	P c a 2 ₁
Unit cell dimensions	a = 25.034(3) Å
	b = 10.4189(13) Å
	c = 12.5096(14) Å
	α = β = γ = 90°
Volume	3262.8(7) Å ³
Z	8
Density (calculated)	3.383 g/cm ³
Absorption coefficient	79.317 mm ⁻¹
F(000)	2880
Theta range for data collection	3.53 to 72.53°
Independent reflections	6111 [R(int) = 0.1058]
Data / restraints / parameters	6111 / 6 / 237
Goodness-of-fit on F ²	2.786
Δ/σ _{max}	14.863
Final R indices [I > 2σ(I)]	R ₁ = 0.2921, wR ₂ = 0.4737
R indices [all data]	R ₁ = 0.2933, wR ₂ = 0.4759
Largest diff. peak and hole	36.761 and -43.921 eÅ ⁻³

^a $R = \frac{\sum ||F_o| - |F_c||}{\sum |F_o|}$, $wR = \left\{ \frac{\sum [w(|F_o|^2 - |F_c|^2)^2]}{\sum [w(|F_o|^4)]} \right\}^{1/2}$ and $w = 1/(\sigma^2(I) + 0.1000P^2)$, $P = (F_o^2 + 2F_c^2)/3$

3.7 Photophysical study of 4-AMPPbI₄:

Here we measured the optical properties such as absorbance and PL of 4-AMPPbI₄ microcrystals. The lowest energy absorption peak is observed at 545 nm, as shown in Figure 13(a). AMPPbI₄ shows the dual PL peaks at 530 nm and 565 nm, as shown in Figure 13(b). The emission at 530 nm is associated with the band edge emission of AMPPbI₄ single crystal, whereas there are no previous reports about 565 nm

emission peak. Comparing both absorbance spectra and PL spectra indicates that the absorption edge states near 545 nm are responsible for the PL peak at 565 nm.

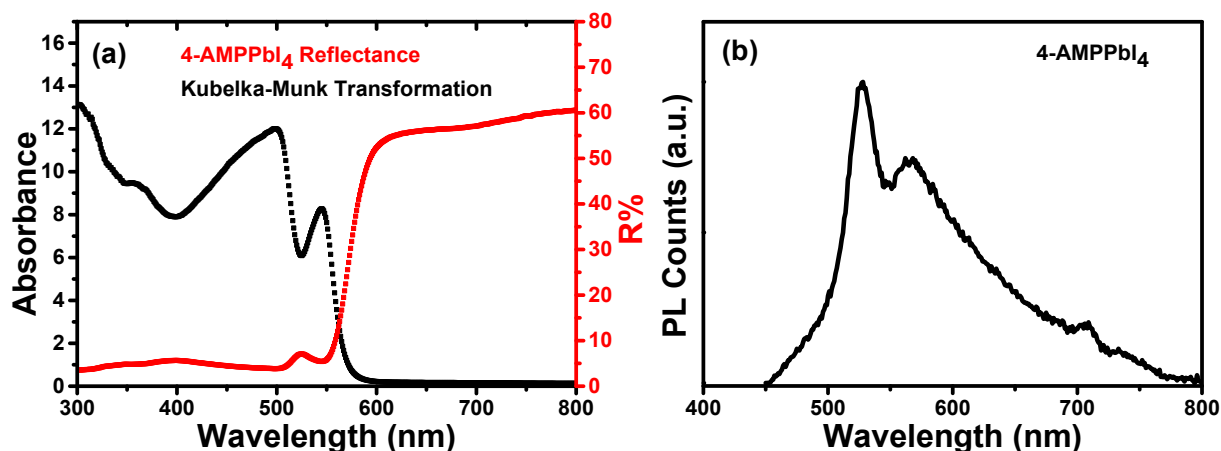


Figure 13. The sample is 4-AMPPbI₄ microcrystals. (a) Recorded reflectance spectrum (red) and corresponding Kubelka-Munk transformation to absorbance spectrum (black) on microcrystals. (b) PL spectrum of microcrystals with excitation at 405 nm.

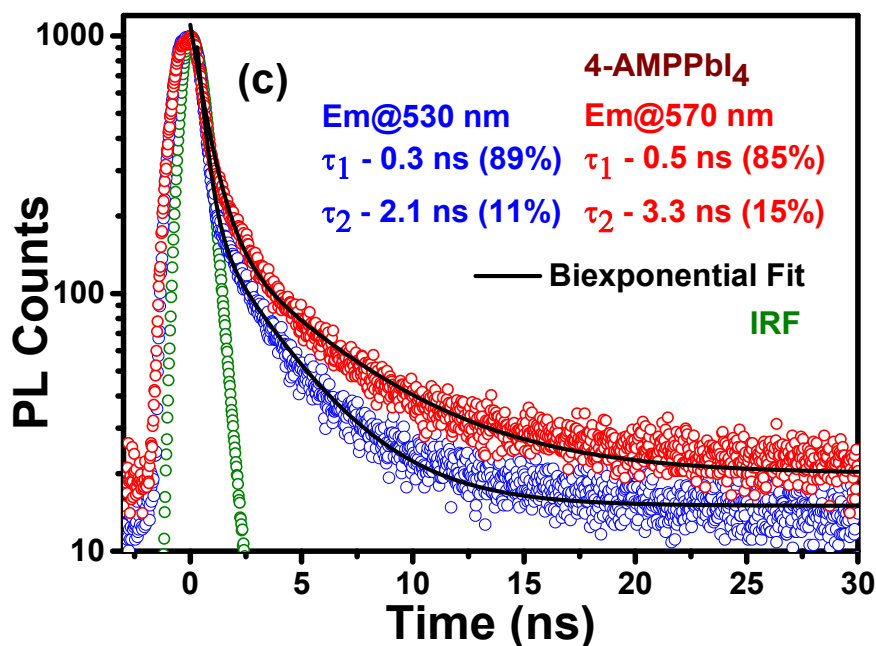


Figure 14. PL decay dynamics recorded at 530 nm (blue) and 570 nm (red) for 4-AMPPbI₄ with excitation at 405 nm.

If 565 nm emission is from defect states, then there would be a low radiative transition probability increasing the PL lifetime. But this is not the case. PL decay measured at 565 nm exhibit the nearly similar lifetime compared to 530 nm emission

(Figure 14). Both the peaks exhibit short lifetimes of few nanoseconds, implying that emissions are probably excitonic in origin with stronger transition probabilities.

3.8 Characterization of 4-AMPSnI₄ single crystals:

After Pb, we moved to Sn-iodide DJ phase hybrid organic inorganic perovskite. Here, we first time successfully synthesized the 4-AMPSnI₄, i.e. (C₆H₁₆N₂)SnI₄ single crystals for the photophysical studies.

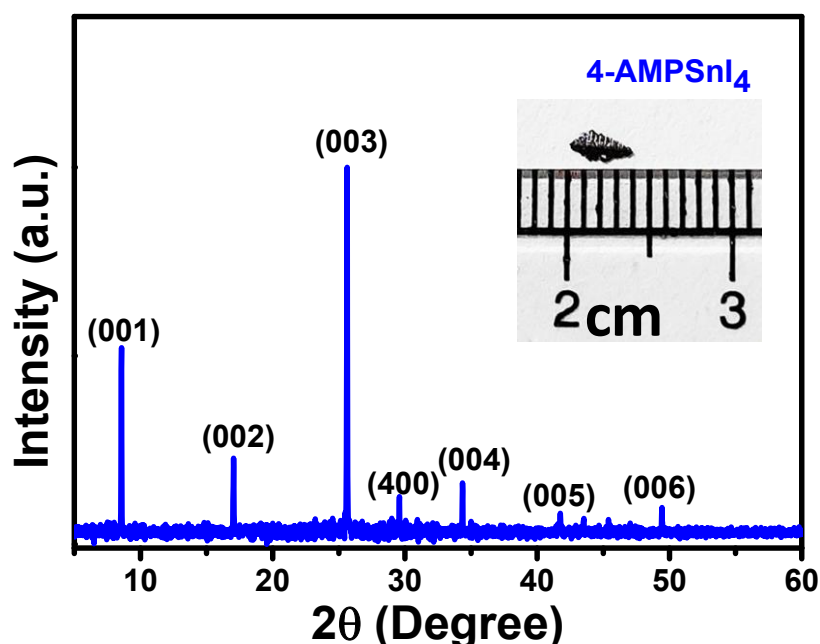


Figure 15. PXRD pattern of 4-AMPSnI₄ single crystal.

Comparing the given 4-AMPSnI₄ PXRD data with the reported 4-AMPPbI₄ single crystal helped us to assign the planes corresponds to the diffraction peaks (Figure 15). Using Bragg's formula $2d\sin\theta = n\lambda$, we calculated the interlayer separation for the (00l) planes is 10.4 Å which is similar to 4-AMPPbI₄. Hence, PXRD data confirmed the phase pure synthesis of the layered 4-AMPSnI₄ single crystal.

3.9 Photophysical study of 4-AMPSnI₄:

Figure 16(a) shows the UV-visible absorption data. PL spectra in Figure 16(b) show two emission peaks at 600 nm and 652 nm with excitation at 405 nm. As previously mentioned, these two emissions are attributed to the bulk and edge of the crystal, respectively. PL decay dynamics confirmed the presence of dual excitonic emission in 4-AMPSnI₄ single crystal which has a nearly similar and shorter lifetime for PL decay (Figure 16(c-d)).

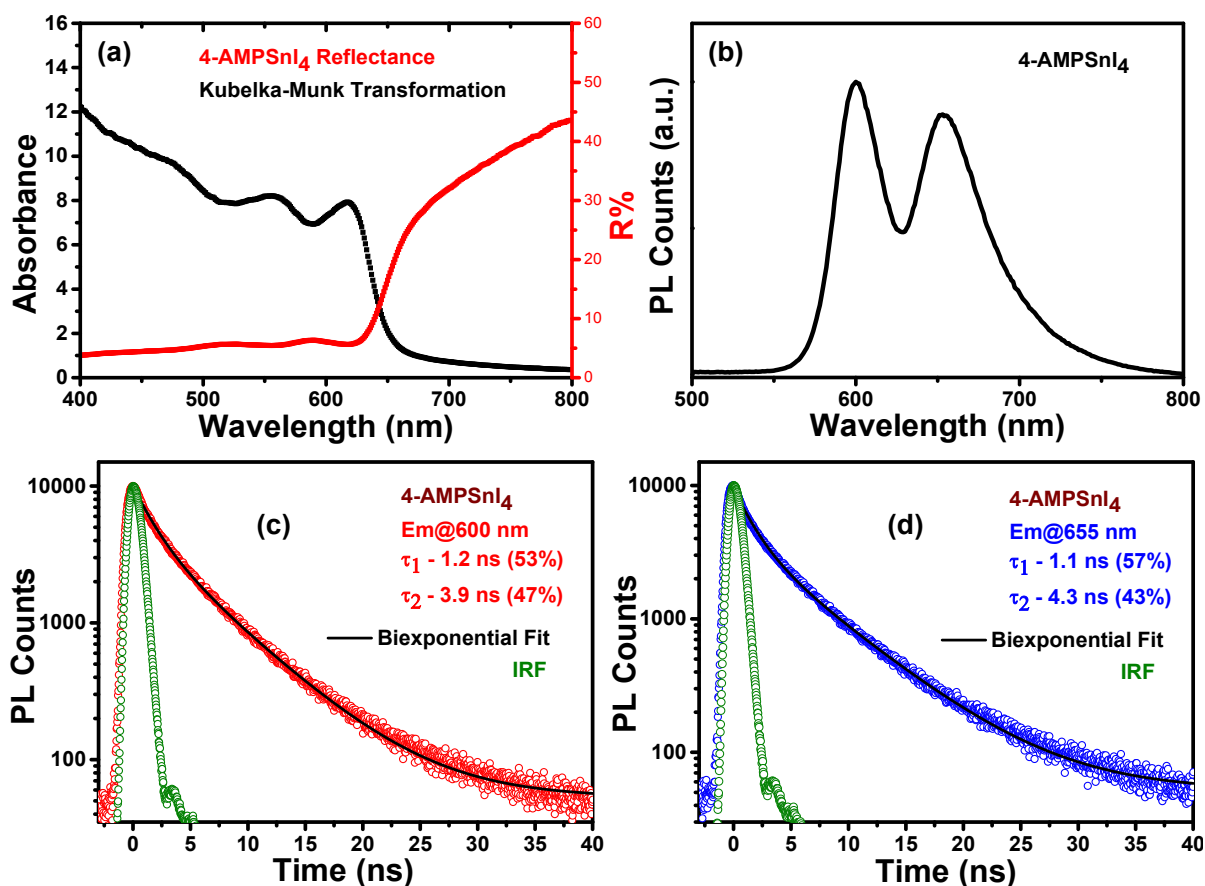


Figure 16. Sample composition is 4-AMPSnI₄. (a) Recorded reflectance spectrum (red) and corresponding Kubelka-Munk transformation to absorption spectrum (black) on single crystals. (b) PL spectrum recorded on millimetre sized single crystal. (c), (d) Measured PL decay dynamics at 600 nm and 655 nm for 4-AMPSnI₄ with excitation at 405 nm.

Table 5. Comparison of dual excitonic emissions for RP and DJ perovskite systems.

DJ Phase	Emission Peaks (nm)		Peak Difference (meV)	RP Phase	Emission Peaks (nm)		Peak Difference (meV)
4-AMPSnI ₄	600	652	165	(PEA) ₂ SnI ₄	625	680	160
4-AMPPbI ₄	528	565	154	(PEA) ₂ PbI ₄	524	560	152

As we know, Rashba splitting in layered perovskites mainly arises due to the presence of heavy metal ion and breaking of inversion symmetry. Reported Rashba splitting value for the 4-AMPPbI₄ is 85 meV³⁴ which is much smaller compared to the

observed 154 meV peak difference (Table 5). Moreover, spin-orbit coupling, in the case of Sn is negligible compare to Pb. However, still, both Sn and Pb analogues show comparable peak difference values which reject the idea of any possible contribution from spin-orbit coupling in dual excitonic emission (Table 5). In analogues systems of Sn and Pb, emission peak difference values for RP and DJ phases are comparable. So we conclude that DJ systems such as 4-AMPPbI₄ and 4-AMPSnI₄ single crystals also show the dual excitonic emission property similar to RP phase even though both phases show structural differences among them.

4. Conclusions

We successfully synthesized the stable (PEA)₂SnI₄ layered hybrid perovskite single crystals. The single crystal of (PEA)₂SnI₄ gives rise to dual excitonic features in PL spectrum. Similarly, single crystals of (BA)₂SnI₄, (HA)₂SnI₄, and (OA)₂SnI₄, which belongs to the same RP phase of layered perovskite show dual excitonic emission. Similar excitonic features have already been observed in the Pb-iodide RP analogues.^{32, 33} This implies that dual excitonic emission is the intrinsic property of all hybrid layered perovskite single crystals in RP phase. Subsequently, we prepared single crystals of 4-AMPSnI₄ and 4-AMPPbI₄ in the DJ phase. These DJ phase single crystals also exhibit the dual excitonic emission. As we point out, emission peak difference values for all the Sn and Pb analogues are comparable, which clearly rules out the possible role of spin-orbit coupling in the observed dual excitonic emission. Since both RP and DJ show similar emission features which imply the dual excitonic emission is independent of organic cation molecules and inorganic layer arrangement. We expect that other metal based 2D layered perovskite single crystals would show similar dual excitonic emission. Understanding this very unusual observation of dual excitonic emission will be critical to understand and optimize optoelectronic applications of hybrid layered perovskites.

References

1. Rose, G., De novis quibusdam fossilibus quae in montibus Uraliis inveniuntur *AG Schade*, **1839**, 3–5.
2. Li, W.; Wang, Z.; Deschler, F.; Gao, S.; Friend, R. H.; Cheetham, A. K., Chemically diverse and multifunctional hybrid organic-inorganic perovskites. *Nat. Rev. Mater.* **2017**, 2, 16099.

3. Mitzi, D. B., Templating and structural engineering in organic–inorganic perovskites. *J. Chem. Soc., Dalton Trans.* **2001**, 1, 1-12.
4. F. S. Galasso, Structure, Properties and Preparation of Perovskite-Type Compounds, Pergamon, New York, **1969**.
5. Shannon, R., Revised effective ionic radii and systematic studies of interatomic distances in halides and chalcogenides. *Acta Crystallogr. Sect. A* **1976**, 32, 751-767.
6. Saidaminov, M. I.; Mohammed, O. F.; Bakr, O. M., Low-Dimensional-Networked Metal Halide Perovskites: The Next Big Thing. *ACS Energy Lett.* **2017**, 2, 889-896.
7. Mitzi, D. B.; Chondroudis, K.; Kagan, C. R., Organic-inorganic electronics. *IBM J. Res. Dev.* **2001**, 45, 29-45.
8. Synthesis, Structure, and Properties of Organic-Inorganic Perovskites and Related Materials. *Prog. Inorg. Chem.*, **1999**, 48, 1-121.
9. <https://www.nrel.gov/pv/cell-efficiency.html>
10. Fabiani, D., Quantifying the Potential for Lead Pollution from Halide Perovskite Photovoltaics. *J. Phys. Chem. Lett.* **2015**, 6, 3546-3548.
11. Niu, G.; Guo, X.; Wang, L., Review of recent progress in chemical stability of perovskite solar cells. *J. Mater. Chem. A* **2015**, 3, 8970-8980.
12. Hao, F.; Stoumpos, C. C.; Cao, D. H.; Chang, R. P. H.; Kanatzidis, M. G., Lead-free solid-state organic–inorganic halide perovskite solar cells. *Nat. Photonics* **2014**, 8, 489-494.
13. Noel, N. K.; Stranks, S. D.; Abate, A.; Wehrenfennig, C.; Guarnera, S.; Haghhighirad, A.-A.; Sadhanala, A.; Eperon, G. E.; Pathak, S. K.; Johnston, M. B.; Petrozza, A.; Herz, L. M.; Snaith, H. J., Lead-free organic–inorganic tin halide perovskites for photovoltaic applications. *Energy Environ. Sci.* **2014**, 7, 3061-3068.
14. Ogomi, Y.; Morita, A.; Tsukamoto, S.; Saitho, T.; Fujikawa, N.; Shen, Q.; Toyoda, T.; Yoshino, K.; Pandey, S. S.; Ma, T.; Hayase, S., CH₃NH₃Sn_xPb_(1-x)I₃ Perovskite Solar Cells Covering up to 1060 nm. *J. Phys. Chem. Lett.* **2014**, 5, 1004-1011.
15. Zuo, F.; Williams, S. T.; Liang, P.-W.; Chueh, C.-C.; Liao, C.-Y.; Jen, A. K. Y., Binary-Metal Perovskites Toward High-Performance Planar-Heterojunction Hybrid Solar Cells. *Adv. Mater.* **2014**, 26, 6454-6460.

16. Hao, F.; Stoumpos, C. C.; Guo, P.; Zhou, N.; Marks, T. J.; Chang, R. P. H.; Kanatzidis, M. G., Solvent-Mediated Crystallization of $\text{CH}_3\text{NH}_3\text{SnI}_3$ Films for Heterojunction Depleted Perovskite Solar Cells. *J. Am. Chem. Soc.* **2015**, *137*, 11445-11452.
17. Bi, D.; Gao, P.; Scopelliti, R.; Oveisi, E.; Luo, J.; Grätzel, M.; Hagfeldt, A.; Nazeeruddin, M. K., High-Performance Perovskite Solar Cells with Enhanced Environmental Stability Based on Amphiphile-Modified $\text{CH}_3\text{NH}_3\text{PbI}_3$. *Adv. Mater.* **2016**, *28*, 2910-2915.
18. Jiang, W.; Ying, J.; Zhou, W.; Shen, K.; Liu, X.; Gao, X.; Guo, F.; Gao, Y.; Yang, T., A new layered nano hybrid perovskite film with enhanced resistance to moisture-induced degradation. *Chem. Phys. Lett.* **2016**, *658*, 71-75.
19. Smith, I. C.; Hoke, E. T.; Solis-Ibarra, D.; McGehee, M. D.; Karunadasa, H. I., A Layered Hybrid Perovskite Solar-Cell Absorber with Enhanced Moisture Stability. *Angew. Chem, Int. Ed.* **2014**, *53*, 11232-11235.
20. Hattori, T.; Taira, T.; Era, M.; Tsutsui, T.; Saito, S., Highly efficient electroluminescence from a heterostructure device combined with emissive layered-perovskite and an electron-transporting organic compound. *Chem. Phys. Lett.* **1996**, *254*, 103-108.
21. Cheng, B.; Li, T.-Y.; Maity, P.; Wei, P.-C.; Nordlund, D.; Ho, K.-T.; Lien, D.-H.; Lin, C.-H.; Liang, R.-Z.; Miao, X.; Ajia, I. A.; Yin, J.; Sokaras, D.; Javey, A.; Roqan, I. S.; Mohammed, O. F.; He, J.-H., Extremely reduced dielectric confinement in two-dimensional hybrid perovskites with large polar organics. *Commun. Phys.* **2018**, *1*, 80.
22. Hong, X.; Ishihara, T.; Nurmikko, A. V., Dielectric confinement effect on excitons in PbI_4 -based layered semiconductors. *Phys. Rev. B* **1992**, *45*, 6961-6964.
23. Stoumpos, C. C.; Cao, D. H.; Clark, D. J.; Young, J.; Rondinelli, J. M.; Jang, J. I.; Hupp, J. T.; Kanatzidis, M. G., Ruddlesden–Popper Hybrid Lead Iodide Perovskite 2D Homologous Semiconductors. *Chem. Mater.* **2016**, *28*, 2852-2867.
24. Lanty, G.; Bréhier, A.; Parashkov, R.; Lauret, J. S.; Deleporte, E., Strong exciton–photon coupling at room temperature in microcavities containing two-dimensional layered perovskite compounds. *New J. Phys.* **2008**, *10*, 065007.
25. Ishihara, T.; Takahashi, J.; Goto, T., Optical properties due to electronic transitions in two-dimensional semiconductors $(\text{C}_n\text{H}_{2n+1}\text{NH}_3)_2\text{PbI}_4$. *Phys. Rev. B* **1990**, *42*, 11099-11107.

26. Liu, X.; Chanana, A.; Huynh, U.; Xue, F.; Haney, P.; Blair, S.; Jiang, X.; Vardeny, Z. V., Circular photogalvanic spectroscopy of Rashba splitting in 2D hybrid organic–inorganic perovskite multiple quantum wells. *Nat. Commun.* **2020**, *11*, 323.
27. Zhao, Y.-Q.; Ma, Q.-R.; Liu, B.; Yu, Z.-L.; Yang, J.; Cai, M.-Q., Layer-dependent transport and optoelectronic property in two-dimensional perovskite: (PEA)₂PbI₄. *Nanoscale* **2018**, *10*, 8677-8688.
28. Kepenekian, M.; Robles, R.; Katan, C.; Saponi, D.; Pedesseau, L.; Even, J., Rashba and Dresselhaus Effects in Hybrid Organic–Inorganic Perovskites: From Basics to Devices. *ACS Nano* **2015**, *9*, 11557-11567.
29. Wang, J.; Zhang, C.; Liu, H.; McLaughlin, R.; Zhai, Y.; Vardeny, S. R.; Liu, X.; McGill, S.; Semenov, D.; Guo, H.; Tsuchikawa, R.; Deshpande, V. V.; Sun, D.; Vardeny, Z. V., Spin-optoelectronic devices based on hybrid organic-inorganic trihalide perovskites. *Nat. Commun.* **2019**, *10*, 129.
30. Straus, D. B.; Hurtado Parra, S.; Iotov, N.; Gebhardt, J.; Rappe, A. M.; Subotnik, J. E.; Kikkawa, J. M.; Kagan, C. R., Direct Observation of Electron–Phonon Coupling and Slow Vibrational Relaxation in Organic–Inorganic Hybrid Perovskites. *J. Am. Chem. Soc.* **2016**, *138*, 13798-13801.
31. Zhai, Y.; Baniya, S.; Zhang, C.; Li, J.; Haney, P.; Sheng, C.-X.; Ehrenfreund, E.; Vardeny, Z. V., Giant Rashba splitting in 2D organic-inorganic halide perovskites measured by transient spectroscopies. *Sci. Adv.* **2017**, *3*, e1700704.
32. Sheikh, T.; Shinde, A.; Mahamuni, S.; Nag, A., Possible Dual Bandgap in (C₄H₉NH₃)₂PbI₄ 2D Layered Perovskite: Single-Crystal and Exfoliated Few-Layer. *ACS Energy Lett.* **2018**, *3*, 2940-2946.
33. Sheikh, T.; Shinde, A.; Mahamuni, S.; Nag, A., Dual excitonic emissions and structural phase transition of octylammonium lead iodide 2D layered perovskite single crystal. *Mater. Res. Express* **2019**, *6*, 124002.
34. Park, I.-H.; Zhang, Q.; Kwon, K. C.; Zhu, Z.; Yu, W.; Leng, K.; Giovanni, D.; Choi, H. S.; Abdelwahab, I.; Xu, Q.-H.; Sum, T. C.; Loh, K. P., Ferroelectricity and Rashba Effect in a Two-Dimensional Dion-Jacobson Hybrid Organic–Inorganic Perovskite. *J. Am. Chem. Soc.* **2019**, *141*, 15972-15976.